Multimodal precision imaging of pulmonary nanoparticle delivery in mice: Dynamics of application, spatial distribution, and dosimetry

Lin Yang[1,2,3], Regine Gradl[4,5,6], Martin Dierolf[4,5], Winfried Möller[1,2], David Kutschke[1,2], Annette Feuchtinger[7], Lorenz Hehn[4,12], Martin Donnelley[13,14], Benedikt Günther[4,5], Klaus Achterhold[4,5], Axel Walch[7], Tobias Stoeger[1,2], Daniel Razansky[3,9,10,11], Franz Pfeiffer[4,5,6,12], Kaye S. Morgan[4,6,8], Otmar Schmid[*,1,2]

[1]Comprehensive Pneumology Center (CPC-M), Member of the German Center for Lung Research (DZL), Munich, 81377, Germany

[2]Institute of Lung Biology and Disease, Helmholtz Zentrum München-German Research Center for Environmental Health, Neuherberg, 85764, Germany

[3]Faculty of Medicine, Technical University of Munich, Munich, 80333, Germany

[4]Chair of Biomedical Physics, Department of Physics, Technical University of Munich, Garching, 85748, Germany

[5]Munich School of BioEngineering, Technical University of Munich, Garching, 85748, Germany

[6]Institute for Advanced Study, Technical University of Munich, Garching, 85748, Germany

[7]Research Unit Analytical Pathology, Helmholtz Zentrum München, Neuherberg, 85764, Germany

[8]School of Physics and Astronomy, Monash University, Clayton, Victoria, 3800, Australia

[9]Institute for Biological and Medical Imaging (IBMI), Helmholtz Zentrum München, Neuherberg, 85764, Germany

[10]Faculty of Medicine and Institute of Pharmacology and Toxicology, University of Zurich, Switzerland

[11]Institute for Biomedical Engineering and Department of Information Technology and Electrical Engineering, ETH Zurich, Switzerland

[12]Department of Diagnostic and Interventional Radiology, Klinikum rechts der Isar, Technical University of Munich, München, 81675, Germany

[13]Robinson Research Institute and Adelaide Medical School, University of Adelaide, Adelaide, Australia

[14]Respiratory and Sleep Medicine, Women's and Children's Hospital, North Adelaide, SA 5006, Australia

*Corresponding author

Dr. Otmar Schmid

E-mail: otmar.schmid@helmholtz-muenchen.de

Tel: +49-89-3187-2557. Fax: +49-89-3187-2400.

Abstract

Targeted delivery of nanomedicine/nanoparticles (NM/NPs) to the site of disease (*e.g.* the tumor or lung injury) is of vital importance for improved therapeutic efficacy. Multimodal imaging platforms provide powerful tools for monitoring delivery and tissue distribution of drugs and NM/NPs. Here, we introduce a preclinical imaging platform combining X-ray (two modes) and fluorescence imaging (three modes) techniques for time-resolved *in vivo* and spatially-resolved *ex vivo* visualization of mouse lungs during pulmonary NP delivery. Liquid mixtures of iodine (contrast agent for X-ray) and/or (nano-)particles (X-ray absorbing and/or fluorescent) are delivered to different regions of the lung via intratracheal instillation, nasal aspiration, and ventilator-assisted aerosol inhalation. We demonstrate that *in vivo* propagation-based phase contrast X-ray imaging elucidates the dynamic process of pulmonary NP delivery, while *ex vivo* fluorescence imaging (*e.g.* tissue-cleared light sheet fluorescence microscopy) reveals the quantitative 3D drug/particle distribution throughout the entire lung with cellular resolution. The novel and complementary information from this imaging platform unveils the dynamics and mechanisms of pulmonary NM/NP delivery and deposition for each of the delivery routes, which provides guidance on optimizing pulmonary delivery techniques and novel-designed NM for targeting and efficacy.

Keywords: X-ray imaging, lung fluorescence imaging, optical tissue clearing, pulmonary delivery, aerosol inhalation therapy

Introduction

Lung diseases are amongst the leading causes of deaths worldwide. According to the World Health Organization (WHO)[1] the chronic obstructive pulmonary disease (COPD) and lung cancer have even been rising from the 4th and 9th in 2000 to the 3rd and 6th of most deadly disease in 2016, respectively. For treatment of lung diseases, direct application of the drug to the lung via aerosol inhalation is widely used due to its high therapeutic index, *i.e.* high efficacy at the site of disease and low side effects in secondary organs. Currently, inhalation therapy is a cornerstone for the treatment of pulmonary infections, asthma, COPD, and cystic fibrosis, but also treatment of lung cancer or even non-pulmonary disease such as diabetes is within reach[2, 3]. Also nanotechnology-enabled drugs (nanomedicines, NM) offer new diagnostic and therapeutic options for cancer and other diseases leveraging their unique features for controlled release, reduced drug toxicity, prolonged residence time and/or targeted delivery [4-6]. Consequently, numerous NM formulations are already in clinical use or are currently undergoing clinical trials[7, 8]. In spite of this success a recent study reported that only about 0.7% of the applied dose of intravenously administered nanoparticles (NPs) accumulates at the tumor sites in animal models[9], suggesting that targeting delivery of NM is still a major subject of both preclinical and clinical studies.

To better understand and optimize drug/NM delivery to the sites of disease within the lung, it is of central importance to quantitatively monitor the dynamic process of pulmonary drug delivery in the context of deposited dose, initial biodistribution, site-specific localization, biokinetics, and therapeutic efficacy (bioactivity) of NM. Non-invasive imaging techniques including magnetic resonance imaging (MRI), single photon emission computed tomography (SPECT), positron

emission tomography (PET), photoacoustic (PA) imaging, ultrasound (US), X-ray based imaging modalities (phase contrast X-ray imaging: PCXI, computed tomography: CT), and optical imaging (*e.g. in vivo* imaging system, IVIS) each provide different advantages in imaging drug/NM distribution, release, and efficacy[10, 11]. MRI provides both morphological and functional information (*e.g.* target site of NM) in the human lung but is limited by poor spatial resolution (*ca.* 1 mm), slow image acquisition, and low sensitivity in the lungs of small animals[12, 13]. Nuclear medical imaging including PET and SPECT offers high sensitivity, high imaging depth, and sufficient dosimetric accuracy for quantitative biodistribution and biokinetics studies in the lung. Since those techniques often need a radiolabeled probe and suffer from poor spatial resolution and lack of anatomical information, hybrid imaging techniques have been proposed to overcome the latter limitations (*e.g.* joint use of SPECT-CT)[10]. Taking advantage of the combined spectral selectivity of molecular excitation by laser light and high-resolution of ultrasound detection[14], PA imaging is an emerging nondestructive hybrid technique (optics and acoustics) that allows deeper tissue visualization of fluorescent agents compared to optical imaging. Similar to US, PA can provide anatomical and dynamic imaging, but it is of limited use for the lung due to restricted ultrasound propagation [15]. Consequently, the penetration depth of light, sensitivity, and quantification ability offered by PA imaging are not sufficient for determination of NM biodistribution and pharmacodynamics in lungs. X-ray based approaches (PCXI and CT) have been recently applied to monitor the pulmonary fluid delivery dynamics and deposition[16-18] and lung pathophysiological state[19] with high temporal and spatial resolution. The major challenges posed by X-ray modalities are that they are incapable of assessing NM bioactivity and for visualizing NM at cellular resolution. Leveraging the wide range of bioactive optical probes noninvasive optical imaging could resolve the bioactivity issue,

but it suffers from poor spatial resolution and low dosimetric accuracy due to strong tissue scattering and absorption of light. There is no single imaging modality that allows for detection of the dynamics of pulmonary drug delivery, regional distribution profile, accurate dosimetry, and cellular localization of NM in intact organ/tissue of animal models.

Multimodal hybrid imaging techniques such as PET-CT and SPECT-MRI are increasingly used as they provide deeper insight into targeting and distribution profile of NM in terms of detection sensitivity, anatomical information, and spatially resolved dosimetry [10, 11, 20]. However, most studies have focused on determining the delivery and therapeutic efficacy of NM to xenograft tumor models in murine models [21, 22], while there is still a lack of understanding of pulmonary drug delivery. In spite of a large number of novel-designed NM with enhanced pharmacokinetic and pharmacodynamic properties[7], such as non-mucoadhesive particles (particles do not adhere to mucus) prolonging lung retention for sustained release of drugs in the lung[23], monitoring the controlled pulmonary delivery of NM in real-time with subsequent analysis of regional spatial distribution, accurate dosimetry, and cellular localization of NM in the lung is still a major unmet need.

This study therefore aims to decipher the dynamics of pulmonary delivery of NPs as well as their regional distribution, dosimetry, and cellular localization by multimodal imaging leveraging X-ray- and fluorescence-based imaging techniques. Lung tissue usually produces low contrast in conventional X-ray images, but the visibility of the lungs can be enhanced using phase-contrast techniques that exploit the phase shift introduced by a sample. For weakly absorbing materials such as soft tissue and air, the difference in the phase shift is significant, which leads to contrast enhancement. Propagation-based phase contract X-ray imaging (PB-PCXI) was chosen here since this technique requires only a single exposure (compared to *e.g.* grating-based phase-

contrast imaging), so it is ideal for imaging dynamic processes [24]. Furthermore, it is a simple technique, because the only change with respect to conventional absorption imaging is an increased sample-to-detector distance and increased source coherence. This coherence requirement usually limits the use of PB-PCXI to synchrotron facilities [25]. In this study the Munich Compact Light Source (MuCLS) was used to produce a sufficiently coherent X-ray beam to obtain edge-enhanced images via PB-PCXI. The acquired images include attenuation and phase information, with the attenuation effects rendering the bones and highly absorbing contrast agents visible, and the phase effects rendering the lungs and airways visible [26]. Here, PB-PCXI was applied to the *in vivo* real-time monitoring of controlled NP-liquid delivery to different regions of the lung, and subsequent *ex vivo* CT and fluorescence imaging (here epifluorescence imaging of the whole or dried-sliced lung or tissue-cleared light sheet fluorescent microscopy, LSFM [27]) further provided the 3D NP distribution profile throughout the entire lung in both a qualitative and quantitative manner. The advantages and limitations of each of these techniques are discussed and we demonstrate the potential of this multimodal imaging platform for resolving mechanisms of pulmonary drug delivery and specific features of the NP distribution profile observed for three of the most widely used preclinical modes of pulmonary application, namely intratracheal instillation, ventilator-assisted aerosol inhalation, and nasal aspiration.

Results

The multimodal imaging approaches presented here provide unprecedented concomitant insights into dose, distribution, and mechanism of pulmonary delivery of drugs at high temporal and spatial resolution. *In vivo* PB-PCXI allows for noninvasive time-resolved monitoring of the dynamic process of drug/nanoparticle delivery, while fluorescence-based *ex vivo* imaging (IVIS and tissue-cleared LSFM) offers quantitative dosimetry and accurate 3D localization of fluorescent tracers (here NPs) with cellular resolution at one time point. Each of these methods requires the presence of either radio- or fluoroactive substances. Here a variety of NPs and molecular substances are used, including the clinically approved iodine as well as gold NPs, iron oxide particles, QDs for X-ray imaging as well as QDs and polystyrene-SkyBlue and melamine resin NPs for fluorescence-based imaging (Table 1). Except for QDs, which are both X-ray absorbing and fluorescent, all other substances require co-application of two contrast agents. The insoluble particles used here have a diameter between 18 nm and 900 nm with a relatively narrow size distribution (geometric standard deviation <1.4, Figure S1).

A schematic overview of the various imaging modalities is presented in Figure 1. During the pulmonary delivery process time-resolved *in vivo* PB-PCXI was performed and mice were sacrificed immediately after completion of delivery, lungs were perfused (removal of blood), and then excised. Subsequent *ex vivo* imaging was performed on the very same lungs using either LSFM on tissue-cleared lungs or X-ray imaging (CT scan) followed by two IVIS fluorescence imaging modalities on dried lungs, namely whole lung fluorescence imaging (WLFI) and lung slice fluorescence imaging (LSFI).

Time-resolved *in vivo* monitoring of controlled pulmonary NP delivery with PB-PCXI

For analysis of the mechanisms involved in pulmonary drug delivery (here: iodine-NP) the temporal evolution of drug accumulation in the different regions of the lung was monitored for various forms of drug application in real-time by PB-PCXI. The intratracheal instillation and X-ray imaging setup is depicted in Figure 1a. As described by Gradl *et al.*[24], mice were fixed in an upright position, mechanically ventilated and an iodine-polystyrene NP suspension was instilled slowly into the lungs using a remotely controlled syringe pump. This permits delivery of a known amount of liquid at a controllable and constant rate (here 4.2 µl/s, *i.e.* 100 µL within 24 s). Triggered by the ventilator, one image per breath was captured during an end-inspiratory breath-hold phase, which minimizes inflation/deflation induced blurring effects [24]. This allowed for time-resolved visualization of the pulmonary NP delivery process. Since intratracheal instillation is typically performed by rapid manual emptying of a syringe (within less than 1 s), we thus refer to the instillation process used here as "slow-instillation".

Figure 2a shows the X-ray images obtained with this setup. The rib cage and spinal cord of the mouse (dark structures) as well as the lung (bright area within the rib cage) enclosing the heart (dark region in the top center of the lung region) are clearly visible. By subtraction of the pre-delivery image from each image during substance delivery a difference image is obtained, which reduces the "background" signal from the rib cage, spine, and heart (Figure 2b). Consequently, this difference image more clearly shows the pulmonary distribution of the iodine-NP liquid, which in this case was directed to the left half of the lung by placing the intubation cannula beyond the first bronchial bifurcation (separating left and right half of the lung). Moreover, the subtraction image also highlights the position of the main bronchi and boundaries of the lung, which provides guidance on localization of the delivered iodine-NP solution which is useful for data interpretation. Figure 2c-2e display equivalent images for different delivery experiments via

intratracheal instillation directed to the right upper, right lower and whole lung, respectively, *via* proper positioning of the inserted cannula. Moreover, intensity profiles along (linear) trajectories across the 2D lung images depicted in Figure 2b-2e illustrate the variability of the grey-scale signal for the different regions of these lungs, where lower signals correspond to regions of higher iodine dose (high X-ray absorption), indicating the major locations of iodine-NP liquid (Figure 2f). This pixel-by-pixel analysis (pixel size: 10.4 µm) reveals massive loss of X-ray intensity in regions of substantial iodine deposition, while the fluctuations in signal originate from artifacts due to *e.g.* imperfect background subtraction partially due to unavoidable slight position changes of the breathing mouse during the course of the substance delivery process.

Time-resolved *in vivo* visualization of the dynamic process of liquid delivery via intratracheal instillation to the lung (see Video S1 and S2 for left and whole lung delivery) reveals that the main delivery mechanism is not only gradual spreading of the liquid from the point of entry (trachea/primary bronchus) to the more distal parts of the lung, but also by recurring liquid accumulation in and blocking of one of the airways followed by rupturing of the liquid blockage during breathing activity. This results in secondary spray/aerosol formation, which provides an efficient mechanism for bulk liquid reaching the distal parts of the lung.

Ex vivo **multimodal imaging of NP distribution in the lungs**

After *in vivo* PB-PCXI each lung underwent *ex vivo* imaging using either LSFM or CT scanning followed by WLFI and LSFI (Figure 1b and 1c). Both imaging modes are mutually exclusive, since the former requires wet fixation and optical tissue clearing, while the latter involves drying of the lung. Since the last *in vivo* PB-PCXI image corresponds to the *ex vivo* images, the agreement between *in vivo* PB-PCXI and *ex vivo* imaging modalities can be assessed. Figure 3

presents an example of this data set after slow-instillation of 100 µL iodine-NP solution. The pseudo-colored PB-PCXI difference image which is overlaid with a directly obtained image clearly indicates two main regions of iodine-NP deposition, one in the upper right lung and the other around the diaphragm (Figure 3a and Video S3). 3D reconstructed *ex vivo* lung from a CT scan of the same subject depicts a qualitatively consistent distribution profile with preferential right superior lobe targeting and some near-diaphragm post-caval lobe deposition (Figure 3b and Video S4). This distribution pattern is also found by WLFI (Figure 3c and Figure S2) and LSFI (Figure 3d).

Ex vivo fluorescence LSFI allows for quantitative analysis of the regional targeting of fluorescence substances. Lungs from 9 independent slow-instillation experiments were stratified for preferentially left and right as well as uniform (global) NP deposition in the lung. The ratios of the fluorescence intensities from the right and left lung, which are normalized to their respective right and left lung volume to account for the effect of volume-dependent lung ventilation[27, 28], reveal that for global delivery the ratio is equal to unity and a 3.7-fold preferential targeting of the right (3.7) and left (3.7 = 1/0.27) half of the lung was accomplished, respectively (Figure 3e). Finally, the delivered dose was determined from quantitative fluorescence analysis using dose-intensity conversion curves based on 2 reference lungs containing known amounts of polystyrene-SkyBlue NPs (using regular intratracheal instillation) and 3 non-treated lungs for tissue-autofluorescence correction[27, 29]. In this context it is important to note that the presence of iodine did not affect the fluorescence signal from SkyBlue NPs (Figure S3). In the present experiments, 50 and 100 µl were applied via intratracheal slow-instillation at a constant delivery rate of (4.2 µl/s) and 72.98 ± 36.21% and 79.9 ± 24.1% of the nominal dose was delivered to the lung, respectively (Figure 3f), where for one of the 50 µL

lungs almost nothing (<7%) reached the lung probably due to accidental withdrawal of the intubation cannula during the delivery procedure. Hence, no significant difference in deposited fraction of applied dose/volume was found for different volumes via slow-instillation (between 50 µL and 100 µL). It also reveals that slow-instillation of 50 µL liquid yields the same fractional deposition as reported for regular instillation 77.2 ± 14.2% (50 µl in < 1 s; no data for 100 µl are available)[29]. Quantitative analysis with any of the other imaging modalities is difficult due to substantial tissue attenuation for whole lung fluorescence imaging and signal saturation (complete absorption of X-ray signal) for X-ray imaging modalities.

In summary, this analysis shows that *in vivo* X-ray and *ex vivo* X-ray and fluorescence imaging approaches show qualitatively consistent pulmonary deposition patterns for intratracheal slow-instillation, which indicates co-localization of X-ray- and fluorescence-active agents. Moreover, LSFI allows for quantitative dosimetry analysis of fluorescent NPs. The data presented here also show that positioning of the intubation cannula beyond the first bifurcation of the bronchial tree allows for regional targeting of liquid substances into the left or right half of the lung, but deliberate selection of either the right or left half is difficult. Finally, regular and slow-instillation provide similar substance delivery efficiency (ca.75%) with somewhat better dose reproducibility for regular instillation.

Visualization of small-volume slow-instillation by multimodal imaging

Visualization of extremely small amounts of bulk liquid (4 µL) delivery throughout the entire murine lung with *ca.* 1000µL total lung volume (600 cm^2 epithelial surface area) via intratracheal instillation is notoriously difficult. It has been reported that addition of lung surfactant could facilitate pulmonary delivery both in terms of speed of dispersion and

uniformity of distribution as surfactant is known to reduce surface tension of the applied bulk liquid[30]. In this case, the mouse was intubated for syringe-assisted slow-instillation, but breathing spontaneously and *in vivo* X-ray image acquisition (100 ms per breath) near the end of inhalation was triggered by monitoring the motion of the chest with an optical displacement sensor[31]. *In vivo* PB-PCXI revealed that delivery of 4 μL of iodine-polystyrene NP liquid resulted in highly localized, small puddles of liquid into either the right or left lung, but not to both sides (Figure 4a and Video S5). Only the proximal bronchial region was reached and addition of surfactant did not affect delivery speed or localization of the liquid as shown in Figure 4d and Video S6. The small amounts of iodine delivered to the lungs were below the detection limit of *ex vivo* CT as seen from Figure 4b and 4e. On the other hand, *ex vivo* WLFI was able to detect the fluorescence signal in the left half of the lung (red in Figure 4c and 4f) confirming the distribution observed with *in vivo* PB-PCXI. Quantitative dosimetry based on LSFI (Figure 4g) revealed no statistically significant effect of lung surfactant on in the delivered dose fraction of 4 μL iodine-NP liquid (with and without surfactant: 0.71 ± 0.19 and 0.53 ± 0.28, respectively). In fact this delivery fraction is also consistent with the corresponding values for 50 and 100 μl of liquid instillation (Figure 3f).

Real-time monitoring of particle delivery by PB-PCXI: gold, iron oxide, and QDs delivery

In the experiments reported above iodine was added to the NP suspension, since the polystyrene NPs cannot be detected by X-ray analysis. Substances with a high atomic number or density, such as iodine-, lanthanide-, gold-, or bismuth-based materials, are preferable used as X-ray contrast agents because of their high absorption cross section[32]. Recently, utilization of NP-

based X-ray contrast agents has been intensively discussed for diagnostic and molecular imaging, as NPs provide the potential of high loading of contrast agents and the possibilities of surface modification enhancing cell/organ-specific targeting. Traditionally, gold NPs have been used as X-ray contrast agents for *e.g.* imaging tumor targeting of NPs *via* proper surface functionalization after intravenous injection *in vivo* [33]. However, gold NPs have rarely been used as X-ray contrast agent for pulmonary delivery. This study visualizes the dynamic process of pulmonary delivery of three types of particles (two out of three are NPs) in real time using *in vivo* PB-PCXI.

Figure S4 shows five consecutive PB-PCXI frames revealing the temporal evolution of the NP delivery process during nasal aspiration of 40 µL gold NP suspension (delivered to one nostril of the mouse with a rate of 0.16 µL/s). The pseudo-colored difference images highlight the location of the NP suspension. The gold NP suspension initially forms an increasing drop at the tip of the syringe and -once large and close enough to the nostril- the droplet is suddenly inhaled (aspirated) and deposited in the left half of the nasal airways and eventually draining down passed the glottis into the trachea into the left primary bronchus as observed in Video S7 and even into the deep lung. The sequence of images in Figure 5a and 5b display the temporal evolution of NP delivery into the deep lung via intratracheal slow-instillation of 100 µL of a mixture of iron oxide & (fluorescent) melamine particles and pure QDs, respectively. Clearly, the iron oxide particles (2.5 mg/mL) were delivered quite uniformly throughout the targeted left half of the lung (Figure 5a), albeit the image contrast is not as good as for iodine (92.5 mg/mL), which is at least in part due to the lower mass concentration/dose of iron oxide particles. The QDs were delivered to the whole lung (Figure 5b) and the mechanism of delivery is a relatively slow and continuous transport (several seconds) of a film of particle liquid (position indicated by arrow) from the

trachea to the deeper regions of the lung. Also, similar to iron oxide, the lower mass dose of QDs (0.4 μM) results in lower contrast compared with iodine (92.5 mg/mL). Relatively uniform distribution of QDs throughout the lung into the distal airways and alveoli makes it even difficult to visualize. The dynamic processes of instillation delivery for iron oxide particles and QDs are shown in Video S8 and S9, respectively. Of note, QDs are particularly interesting, as they can serve as contrast agent for both X-ray and fluorescence imaging.

Cellular localization of NPs revealed by *ex vivo* tissue-cleared LSFM in non-dissected lungs

None of the imaging modalities above offers the possibility for three-dimensional visualization of NP localization with cellular resolution throughout the entire mouse lung. While CT scan and LSFI offer 3D imaging capabilities, they do not allow for NP localization within individual cells. We recently demonstrated that *ex vivo* LSFM allows for quantitative co-mapping of lung architecture and NP deposition with single-cell resolution in non-dissected but optically cleared lungs[27]. Here we apply this method to study the pulmonary distribution of 100 μL of a NP suspension after intratracheal slow-instillation. Figure 6 shows the general agreement of the whole lung distribution as observed by PB-PCXI and LSFM for iodine-melamine NPs (Figure 6a and 6b), iron oxide-melamine NPs (Figure 6d and 6e) and QDs (Figure 6g and 6h). At cellular resolution (pixel size < 1 μm) melamine NPs were found mainly deposited in the bronchi as well as the bronchioles and proximal part of the alveolar duct (Figure 6c), the so-called proximal acinar region. Similar results were found for iron oxide and (fluorescent) melamine NPs delivery however with a more preferential delivery to the left half of the lung distribution (Figure 6d and 6e). Also the small amount of melamine NPs delivered to the right lung were preferentially located in the distal small airways (bronchioles) and proximal alveolar region (entrance of alveolar sac) (Figure 6f). Finally, Figure 6g displays the QDs distribution profile in the whole

lung imaged by PB-PCXI and the regions of high QD dose are indicated by red arrows. It is evident that in this case QDs were distributed to all 5 lung lobes but did not transport into the peripheral lung (Figure 6h) reaching only a few localized small alveolar regions (Figure 6i). An animation of the distinct 3D distribution profiles of QDs in whole murine lung measured by LSFM can be seen in Video S10.

Multimodal imaging for comprehensive deciphering the characteristics of aerosol inhalation

The clinically most relevant route of pulmonary drug delivery is aerosol inhalation. Here an iodine-NP liquid was delivered to the lung via ventilator-assisted inhalation of aerosols. Since individual aerosol droplets are too small for direct imaging (2-4 µm diameter) and their liquid/contrast delivery rate was extremely small (8.6 nL/s; ca. 490-fold smaller than slow-instillation), *in vivo* PB-PCXI is very challenging. In order to visualize the dynamic delivery process of aerosol inhalation, a large volume of NP-iodine liquid was nebulized (225-300 µL) and quantitative fluorescence spectroscopy in tissue homogenates revealed that 3.7 ± 1.1% and 5.6 ± 2.3% of the applied volume was deposited in the lung lobes and the trachea, respectively (Figure 7j)[34]. It is noteworthy that from quantitative spectrofluorometry of the lung slices (LSFI) one obtains a deposited aerosol fraction of 15.6 ± 2.8 % (whole lung) (Figure 7j), which significantly larger than the 9.3 ± 2.3% (trachea + lung lobes) measured in lung/trachea homogenates, probably due to the higher light attenuation in sliced lung tissue. Since we consider tissue homogenization as more accurate the method of LSFI[27, 34], we report 8.6 nL/s and 12.9 nL/s as pulmonary and tracheal aerosol deposition (delivery) rate, resulting in 5.6 µL and 8.3 µL NP liquid out of applied 150 µL volume deposited in the lung and trachea, respectively. Not surprisingly, *in vivo* PB-PCXI showed no iodine-related signal during aerosol

application (Figure 7a) due to the low iodine delivery rate and the extremely uniform distribution of (aerosolized) iodine throughout the lung. On the other hand, gradual accumulation of iodine in the lung over the entire inhalation period (10 min 48 s) was sufficient for obtaining a clear iodine signal from *in vivo* PB-PCXI (Figure 7a-d and Video S11).

Moreover, *in vivo* PB-PCXI was useful to resolve unexpected, non-aerosol related secondary liquid re-distribution mechanisms which can occur during ventilator-assisted aerosol inhalation. Unlike instillation, which shows a relatively patchy liquid distribution in the lung (Figure 6b), aerosol inhalation spreads the relatively small lung-deposited dose uniformly throughout the entire lung as can be clearly seen from *ex vivo* 3D reconstruction of the lung from CT scan (Figure 7e), *ex vivo* WLFI (Figure 7f) and *ex vivo* tissue-cleared LSFM (Figure 7g, h and i). During the process of ventilator-assisted inhalation localized accumulations of liquid were observed in the upper airways near the trachea (Figure 7b, arrow), which were gradually transported to the lower airways (Figure 7c, arrow) and into the bronchiolar region where they dispersed (Figure 7d, arrows) into even smaller liquid accumulations as evidenced by fluorescence "hot spots" seen in LSFM (Figure 7h, arrows). Not only the presence but also the origin of these occasional accumulations of liquid in the lower bronchial region can be understood from multimodal imaging. *Ex vivo* whole lung imaging (Figure 7f and g) and quantitative fluorometric dosimetry (Figure 7j) provide evidence for substantial aerosol deposition in the trachea (ca. 60% of the total deposited aerosol dose is deposited in the trachea). Since the murine trachea is a rather narrow duct, it is conceivable that the trachea-deposited aerosol will eventually block the trachea resulting in spill-over of some of the liquid in the trachea into the upper airways and from there into the bronchiolar region as observed by *in vivo* PB-PCXI (Figure 7b-d) and *ex vivo* LSFM (Video 12). As this spill-over typical occurred after

95s during nebulization, we conclude that at least 1.2 µL (12.9 nL/s · 95 s) of liquid has to get accumulated in the trachea for occurrence of the spill-over, which corresponds to 22 µL of nebulized liquid (=1.2 µL/0.056).

Discussion

Aerosol delivery of drug/NM is the most widely used application route for treatment of lung disease [35, 36]. Targeted delivery of drug/NM on a regional and even cellular scale is of central importance for precision medicine especially for localized lung diseases such as lung cancer, asthma, emphysema or COPD [3, 37]. Also inhalation of ambient NPs is one of the main health hazards associated with NPs [38, 39]. The region of NM/NP deposition can have a significant impact on residence time, release kinetics and hence bioactivity of the drug or toxicity of NPs[40, 41]. While NM/NP can be quickly (within minutes) removed from the upper airways by mucociliary transport, clearance of NM/NP from the alveolar epithelium mainly relies on uptake by alveolar macrophages (takes a few hours), which may be enough time for direct bioactivity/toxicity of the NM/NP or result in secondary drug release into or from the macrophages[2]. Consequently, understanding the mechanisms of pulmonary NM/NP delivery and their relevance for tissue-delivered NM/NP dose with cellular resolution is essential for the development of effective NM [42] or minimizing health hazards of NPs[43]. Standard histological analysis or single-modality imaging techniques cannot resolve the entire delivery process in all relevant temporal (seconds to days) and spatial scales (whole lung to cellular)[44]. This is also the case for the preclinical efficacy or toxicity testing of NM/NP using animal models.

In this study we combined *in vivo* X-ray and *ex vivo* fluorescence imaging modalities to investigate the dynamic process of pulmonary NM delivery and its impact on pulmonary NM distribution with high temporal and spatial resolution in murine lungs. PB-PCXI utilizes differences in X-ray refractive index and associated phase shifts at air-tissue interfaces for enhancing soft tissue contrast (*e.g.* in the lung) as compared to X-ray absorption [26]. Building on our previously published *in vivo* PB-PCXI studies in murine lungs[18, 24], the present study

demonstrates that combined *in vivo* PB-PCXI and *ex vivo* fluorescence imaging can provide complementary information which enhances the understanding of complex processes such as NM/NP delivery to the lung in a quantitative way on various scales (whole lung to cellular). The strengths and weaknesses of all five imaging modalities used here are summarized with respect to 2D/3D imaging capability, resolution, fidelity (conservation of original anatomical 3D structure), anatomical information and technical complexity as summarized in Table 1. In general, X-ray imaging is used here for *in vivo* imaging at high temporal resolution (1 Hz), while *ex vivo* fluorescence imaging provides insight into spatially resolved dosimetry.

In preclinical lung research, instillation or aspiration of bulk liquids are the most widely used methods of pulmonary drug delivery. On the other hand, aerosol inhalation - not bulk liquid application - is the preferred route of drug delivery in clinical settings. In spite of their widespread use detailed information on the dynamic details of the application processes and spatially resolved dosimetry is scare. All three application routes have been investigated in this study, but a significant focus was on ventilator-assisted aerosol inhalation, since it offers a technologically mature, efficient (ca. 4% of invested dose is delivered to lung) and dose-controlled method for physiologic delivery of liquid substances to the lungs of animal models (here: mice) using a commercially available device (flexiVent system, EMKA/SciReq Inc.). As such it has the potential to at least partially replace intratracheal instillation and nasal aspiration in future preclinical inhalation drug or toxicity testing.

It is evident, that intratracheal instillation allows for highly efficient (76.3 ± 23.0% of invested dose reaches the lung), dose-controlled delivery of liquids (repeatability: 30.1%) for all tested liquid volumes (4-100 µL) into the deep parts of the lung (bronchioles and even alveoli). It is not intuitively clear how a bulk liquid injected into the trachea via intratracheal instillation can reach

the deeper parts of the lung. *In vivo* PB-PCXI revealed that the instilled bulk liquid is not primarily flowing down the bronchial tree, but is distributed quite uniformly throughout the lung by secondary aerosol formation due to occasional blockage of the airways with liquid and subsequent bursting of this blockage during breathing activity (Video S1-S3)[24]. As mentioned above, the slow-instillation process (24 s for 100 µl; 4.2 µL/s), which was used here for the sake of *in vivo* PB-PCXI imaging, is not identical to the typically used, rapid manual instillation (<1 s, >50 µL/s). However, the main features of pulmonary fluorescence distribution and the measured delivery efficiency (76.3 ± 23.0%) is in excellent agreement with observations for rapid instillation (77.2 ± 14.2%) as provided by Barapatre *et al*. [29]

In vivo PB-PCXI also provides valuable insights into the mechanisms of pulmonary NM/NP delivery via ventilator-assisted aerosol inhalation. As expected there is a very gradual, uniformly distributed increase in X-ray signal with no burst-like events as seen for intratracheal instillation, which is related to aerosol deposition in the lung occurring uniformly at a relatively low delivery rate. However, even for ventilator-assisted aerosol inhalation we observed occasional localized accumulations of liquid in the upper airways near the trachea, which were gradually flowing down the airway tree reaching even the bronchiolar region (Figure 7b-7d). Fluorescence imaging and fluorescence-based dosimetry revealed that a large fraction of the aerosol dose is deposited in the trachea (ca. 60% of total deposited dose) due to the spray-like aerosol stream exiting the narrow intratracheal intubation cannula. Since direct aerosol deposition in the bronchial tree would result in a more gradual process of liquid accumulation, spill-over from the trachea is the most likely reason for this to occur. From the measured deposition rate (based on fluorescence) and the time of first occurrence of liquid accumulation in the airways (*in vivo* PB-PCXI), we determined that this non-aerosol related transport effect occurs if more than 22 µL of liquid is

nebulized. The critical liquid volume of 22 µL is expected to depend on positioning of the mouse and on ventilation parameters (breathing frequency, tidal volume, length of breathhold, inhalation-to-exhalation time ratio). In our case, the mouse was held in upright position (for the sake of *in vivo* PB-PCXI), while for typical aerosol applications the mouse is laying horizontally on its back. Therefore, we recommend nebulizing as little volume as possible with the flexiVent ventilation system to avoid non-aerosol related lung delivery processes. However, even with this artifact the delivery of NPs to the lung is much more uniform with ventilator-assisted aerosol inhalation than with intratracheal instillation on a whole lung, regional, generation and cellular scale. It is important to note that the initially unexpected fluorescence "hot spots" detected with LSFM in the deeper bronchial region (Figure 7h), could not have been explained without the information provided by *in vivo* PB-PCXI.

A prerequisite for combing X-ray and fluorescence imaging is that the co-applied active agents (X-ray absorption and fluorescence activity) have the same deposition profile in the lung. Since both agents are applied as liquid mixture, this is to be expected. This was confirmed for all contrast/fluorescence agents/mixtures used here (Table 1) - not just the clinically approved iodine - as evidenced by the excellent qualitative agreement of the spatial distribution profiles for all imaging models covering different volumes (4-100 µL), different localization (left, right, whole lung) and different degrees of spatial uniformity (patchy or uniform) of the applied liquid. QD is the only type of contrast agent (NP) which is both x-ray- and fluorescence-active.

Limitations of the X-ray imaging modalities were mainly related to the signal-to-noise ratio for low amounts of liquid or very uniformly distributed contrast agents. For instance *ex vivo* CT reached its detection limit for localized delivery of 4 µL (iodine-NP solution with 92.5 mg/mL iodine) of bulk liquid and uniformly distributed aerosol (11 µL) (Figure 4b, 4d and 7e). Also *in*

vivo PB-PCXI was difficult, but not impossible, for the latter case. On the other hand, fluorescence imaging on dried lungs (especially on whole lungs; WLFI) was prone to widen the apparent region of particle deposition due to tissue-related light scattering effects, which can be largely eliminated by tissue clearing combined with LSFM.

As mentioned above, most of the standard imaging modalities (*e.g.* PA, US, CT, SPECT, PET, and MRI) are unable to visualize pulmonary fluid delivery dynamics at 1 Hz under *in vivo* conditions in mice mainly due to the poor spatial and temporal resolution [16]. Recently, some multimodal imaging techniques have been used for determination of NP biodistribution and bioactivity in preclinical research. For instance, a combination of triple imaging techniques (*i.e.* dark-field light microscopy, electron microscopy, and nanoscale secondary ion mass spectrometry) was used to study the NP-interaction with green algae in the context of NP localization, internalization and chemical identity [45]. Also, quantitative imaging of co-localization of tumor associated macrophages with therapeutic ^{64}Cu-labeled polyglucose nanoparticle in an orthotopic model of lung adenocarcinoma was accomplished *via* PET, *in vivo* confocal microscopy, and tissue-cleared LSFM [46]. PCXI has already been applied for *ex vivo* and *in vivo* studies on mucociliary transport of large microparticles or 5-100 μm fibers in the trachea or upper airways of animal models such as mice and pigs[26, 47-49] and for monitoring the delivery of liquids to murine lungs via nose- or intubated cannula-delivery[16-18, 25]. Moreover, several common bulk particulates (*e.g.* lead dust, quarry dust, glass beads, asbestos, and Galena with size $\geq$ 5 μm) were tracked in live animal trachea airways by PCXI, showing the high variability in particle movement during mucociliary transport [26, 47, 50]. A few available NPs with high atomic number such as gold NPs, bismuth NPs, lanthaninde-doped NPs, tantalum pentoxide NPs as new contrast agents of X-ray based modalities have also been studied for diagnostic and

molecular imaging [33]. However, to the best of our knowledge, real-time monitoring of the pulmonary delivery of NP suspensions has not been studied, yet, and the combination of *in vivo* PCXI and quantitative and spatially resolved *ex vivo* fluorescence imaging provided complementary insights into the mechanisms, regional/cellular distribution and dosimetry of pulmonary drug delivery in mice. By virtue of bioactive fluorescent probes fluorescence imaging is also suitable for bioactivity studies [43, 44]. In principle the five modes of imaging presented here can be reduced to two modalities, namely *in vivo* PB-PCXI and one of the three fluorescence imaging modalities, which should be selected based on the experimental constraints (available time for sample and image processing, cost, spatial resolution, *etc*).

The core issue of this study is to decipher the main features of the dynamic delivery process of NPs to the nose/lung and to characterize the initial 3D NP distribution profile immediately after varied routes of pulmonary delivery. Here, NPs were suspended in liquid and delivered either as bulk liquid (nasal aspiration, intratracheal instillation) or droplets (aerosol inhalation). Consequently, the initial deposition profile of NPs mainly depends on liquid properties (*e.g.* delivery rate and droplet size). The more patchy, central deposition of QDs (Figure 6g) as compared to melamine NPs (Figure 6b) could be related to the higher viscosity of QD suspensions [27]. After deposition on the lung epithelium the liquid phase of the NP suspensions will be resorbed by lung tissue and re-distributed of NPs within the lung or out of the lung (biokinetics) will depend on NP properties including size, shape, chemical composition and surface functionalization [51, 52]. These secondary redistribution/biokinetics issues are relevant for many therapeutic and toxicological considerations, but beyond the scope of the present study. Nevertheless, they can be addressed with the imaging platform described here. A generation limitation of this study is the use of mixtures (iodine with Sky Blue, iron oxide with melamine

NPs), which is not favorable for longitudinal study of NP biokinetics in lungs as different components (active agents) possess their own pharmacokinetics. The development of bi-modal contrast agents or novel NP formations suitable for both X-ray imaging and fluorescent imaging allows for combined NP pulmonary delivery and biokinetics studies since it avoids the occurrence of artifacts due to the use of two potentially interacting and/or differently behaving contrast agents. In this study, 20 nm QDs were successfully applied as an example for a bimodal NP. Alternatively, encapsulated or conjugated hybrid particles consisting of one fluorescent and one X-ray-absorbing material, such as iodinated polymers or liposomes with fluorescent dyes have been widely used for bimodal imaging of NP accumulation in tumors [10, 32, 33, 53], could be particularly useful in future pulmonary studies.

Conclusion

In this proof-of-concept study, we introduced and validated a multimodal imaging approach for comprehensive understanding of the mechanisms of pulmonary NP delivery in the context of dynamics of the delivery process, deposited dose, regional distribution, and cellular localization of NP in the (non-dissected) whole murine lung. This imaging platform consists of *in vivo* PB-PCXI, *ex vivo* CT and three *ex vivo* whole- and sliced-lung epifluorescence imaging or *ex vivo* LSFM on tissue-cleared lungs. While each of these imaging modes has strengths and weaknesses, selection of PB-PCXI and LSFM would not result in substantial loss of information. Mixing of particles as contrast agents for X-ray (iodine, gold NPs, iron oxide particles, and QDs) and fluorescence imaging (fluorescently labeled polystyrene or melamine NP and QDs) allowed for time-resolved (1.5 Hz) *in vivo* visualization of the dynamics of the pulmonary particle delivery

process via intratracheal slow-instillation or ventilator-assisted aerosol inhalation with *in vivo* PB-PCXI. Moreover, *in vivo* and *ex vivo* X-ray particle distribution profiles were in good qualitative and quantitative agreement with regional distribution patterns observed with fluorescence imaging techniques. This implies that the two applied contrast are co-localized during and directly after delivery. Our study also reveals that for intratracheal instillation of a bulk liquid the pulmonary distribution does not primarily occur via draining of the liquid down the bronchial tree, but by secondary aerosol formation associated with liquid blockage of airways and subsequent bursting of this blockage during breathing activity. In contrast, time-resolved *in vivo* imaging of the ventilator-assisted aerosol inhalation process revealed slowly accumulating uniform aerosol deposition throughout the lung with occasional transport of bulk liquid into the lung. The latter is likely due to direct impaction of aerosol spray exiting the intubation cannula resulting in liquid accumulation in the trachea and eventual spill-over into the bronchial region of the lung, if more than 22 µl of liquid is nebulized. This spill-over explains the initially unexpected sporadic occurrence of *ca.*100-200 µm hot-spot regions in *ex vivo* LSFM lung images after ventilator-assisted inhalation. Development of bi-modal contrast agents like QDs, which are suitable for both *in vivo* PXCI and *ex vivo* LSFM, are expected to be particularly useful for co-visualization of controlled pulmonary delivery of NP in real time and 3D biokinetics over long term. The present study thus describes a complementary multimodal imaging platform for high temporal and spatial resolution visualization of pulmonary NP delivery in a quantitative manner, which will accelerate the ability to target active-NM/drugs to the diseased region of the lung and enhance the development and efficacy of the novel-designed NM.

Experimental Section

By virtue of concomitant multimodal *in vivo* and *ex vivo* imaging new insights into key aspects of common preclinical and clinical methods for pulmonary substance delivery are presented. The related materials and methods are described including the diverse set of imaging modalities and the panel of methods for pulmonary substance delivery.

Materials

Each of the imaging modalities requires the use of materials with specific radio- or fluoroactivity.

For X-ray phase contrast imaging, a clinically approved iodine-based contrast agent (Ultravist-370, 370 mg iodine/ml) and three types of metal NPs were used, namely gold NPs ((VMD) 20.7 ± 9.7 nm), Roti®-MagBeads (magnetic iron oxide embedded in silicium oxide surface coated with carboxylic groups, VMD: 893.5 ± 348.9 nm, 10 mg/mL, Carl Roth GmbH, Karlsruhe, Germany), and Qdot 800 ITK™ carboxyl quantum dots (QDs emission at 800 nm; VMD: 18.1 nm ± 6.5 nm Invitrogen, Ltd., Paisley, UK). Gold NPs were synthesized according to manufacturer instructions using 6 mg of gold (III) chloride trihydrate ($HAuCl_4 \cdot 3H_2O$, ≥99.9%, Sigma-Aldrich) dissolved in 1 mL of deionized water. Then, 49 mL of water was added and the final gold solution was heated. When the gold solution started boiling, 0.94 mL of a 0.04 mol L^{-1} aqueous solution of sodium citrate ($HOC(COONa)(CH_2COONa)_2 \cdot 2H_2O$, ≥99.0%, Sigma-Aldrich) was added to the gold solution, which was kept boiling for further 5 min. The solution changed color from transparent yellow to transparent grey, then black and finally dark pink. Subsequently, the solution was taken from the heating plate and left stirring for 1 h in the dark, and then stored in the dark until use. The purchased QDs (stock solution: 8 µM) were made from

the crystals of a semiconductor material (CdSeTe), shelled with a ZnS layer and further coated with a polymer layer with carboxylic groups.

For fluorescence-based microscopy, polystyrene NPs with the embedded fluorescent dye SkyBlue (excitation /emission =670 nm/710 nm; VMD: 483.9 nm ± 122.3 nm ; 10 mg/mL; Kisker Biotech GmbH, Steinfurt, Germany), melamine resin fluorescence particles (MF, ex/em= 636 nm/686 nm; VMD: 498 ± 111.4 nm, microParticles GmbH, Berlin, Germany), and QDs were used. The commercial MF NPs (stock suspension: 25 mg/mL) were prepared via an acid-catalyzed polycondensation reaction of melamine resin precondensates in the presence of selected fluorescent dyes in the aqueous phase.

Sizing of nanoparticle suspensions

Hydrodynamic diameter measurement of all NP suspension was performed with dynamic light scattering (DLS) using a Malvern Zeta Sizer Nano instrument (Malvern Instruments Ltd., Malvern, UK) (Figure S1). Of note, The observed increase of about 50% in volume median diameter (VMD) of polystyrene and melamine NPs when transferring them from water to iodine solution (from about 490 nm to 770 nm) (Figure S1) possibly due to iodine-induced agglomeration, did not adversely affect their fluorescence signals, which remained stable for more than a week after mixing (Figure S3).

Animal handling

Wildtype C57BL/6 female mice (age 9-18 weeks, 19-25 g) were housed in individually ventilated cages (IVC-Racks; Bio-Zone, Margate, UK) supplied with filtered air in a 12-h light/12-h dark cycle. Mice were provided with food (standard chow) and water ad libitum. All

procedures involving animal handling and experiments were carried out in accordance with protocols approved by the Regierung von Oberbayern (District Government of Upper Bavaria, AZ55.2–1-54-2532-108.13).

The animals were anesthetized by intraperitoneal injection of a triple combination of medetomidine (0.5 mg/kg body weight), midazolam (5 mg/kg body weight), and fentanyl (0.05 mg/kg body weight). The mice were then intubated by a non-surgical technique using a 20 G cannula with one side inserted into the trachea and the other side connected to a mechanical ventilator (flexiVent FX system, Scireq Inc., Canada), allowing for exact control over the breathing activity of the mouse during pulmonary application of liquids and during *in vivo* acquisition of images.

Methods of pulmonary substance delivery

Three widely used techniques of pulmonary delivery of liquid substances were investigated here, namely intratracheal instillation and nasal aspiration of bulk liquids as well as (ventilator-assisted) inhalation of aerosolized liquids. For each of these methods time-resolved *in vivo* monitoring of pulmonary substance delivery throughout the entire lung was performed with PB-PCXI, which is described in detail below. However, the technical details related to PB-PCXI image acquisition deserve careful attention and are therefore included in this section.

For intratracheal slow-instillation delivery, the setting was similar to that depicted in previous studies [24, 25]. The mice were mechanically ventilated at 90 breaths/min, 30 mL/kg tidal volume and an inhalation-inflation (breath-hold)-exhalation time ratio of 1:1:1. The liquid was introduced by a heat thinned PE10 polyethylene tube that was passed through the flexible wall of the ventilator inspiratory tube. The inner PE tube was small enough not to block the intubation cannula enabling simultaneous liquid delivery and mechanical ventilation. The liquid delivery

(slow-instillation) was remotely controlled by a syringe pump (UltraMicroPump III and Micro4 controller, World Precision Instruments, Sarasota, FL) that allows for both controlled liquid delivery from outside the imaging hutch and consecutive imaging during the whole instillation process. As listed in Table 1, 100 µL of various NP mixtures for combined X-ray and fluorescence imaging (Sky Blue-iodine: 1:20 Sky Blue (stock suspension) and 1:4 iodine; melamine-iron oxide: 1:20 melamine and 1:4 iron oxide NPs) or QDs (1:20 dilution) were continuously delivered via the syringe pump to the trachea in approximately 24 s (4.2 µL/s). PB-PCXI image acquisition was performed triggered by the ventilator at a frame rate of up to 1.5 fps (frames per second) using a 200 ms (100 ms for QDs) exposure during an end of inspiration 222 ms breath-hold phase.

To study the effect of alveolar surfactant (Alveofact 45 mg/mL, Lyomark Pharma GmbH, Germany) on the pulmonary distribution of small amounts of liquids applied via intratracheal instillation, the delivery of a small volume (4 µL in 5 s *i.e.* 0.8 µl/s) of a iodine-NP-surfactant mixture was investigated. The mixture contained 1:4 diluted iodine and 1:20 diluted polystyrene-SkyBlue NPs with (+) or without (-) surfactant (25 mg/mL) in distilled water. For this experiment the mice were spontaneously breathing so the ventilator was replaced with a non-contact fibre optic displacement sensor (RC-60, Philtec, MD) that was configured to detect respiratory motion and deliver an electrical trigger signal for image capture. The frame rate was maintained at 1.5 fps, but the exposure time was reduced to 100 ms to mitigate unavoidable motion blur due to the absence of a breath-hold phase. It is noteworthy that for practical reasons the liquid delivery rates of 4.0 µl/s and 0.8 µl/s are slow compared to typical intratracheal instillation protocols delivering 50-200 µl within < 1 s; by manually emptying a loaded syringe *via* the intubation cannula into the trachea at a delivery rate of >50 µl/s. Since less than 1 s of

delivery time is too short for reliable *in vivo* PB-PCXI imaging of different stages of the delivery process, slower delivery rates were chosen here, and image acquisition was performed as described above.

For ventilator-assisted aerosol inhalation, a similar protocol and setup as described for 100 µL instillation was used (80 breath/min, 30 mL/kg tidal volume, 200 ms and PB-PCXI image acquisition occurred during an end-inspiratory breath-hold phase as described above. In contrast to intratracheal slow-instillation, the inner PE10 polyethylene tube was removed and the ventilator was equipped with a nebulizer (Aeroneb Lab Small, Aerogen Inc., Galway, Ireland) in the inspiratory tubing for the generation and transport of liquid aerosol droplets to the lungs of mice. It has been shown that for the flexiVent system operated under the conditions described above about 4-5% of the nebulized liquid is deposited in the lung (downstream of trachea), the rest deposited in the ventilation tubing or exhaled by the mouse[27]. Moreover, we determined empirically that 150 µL is the maximum liquid volume that can be nebulized without at least partially blocking some part of the inspiratory ventilation tubing by accumulated rain-out. Here, the nebulizer typically generates droplets with a liquid output rate of 0.26 mL/min and a volume-weighted median diameter of 2-4.0 µm. Here, the nebulizer was breath activated and active for 40 ms during the inspiratory phase. For a breathing rate of 80 breath/min this corresponds to an effective liquid output rate of 13.8 µl/min during flexiVent operation. Hence it takes ca.10.8 min (870 breaths) to nebulize 150 µL liquid resulting in 5.6 µL of contrast agent deposited in the lung. (3.7% of applied dose is deposited in the lung), where we relied on the dosimteric results from quantitative fluorescence spectroscopy in lung homogenates rather than the experimentally more uncertain LSFI results[34] (Figure 7g). The aerosol delivery rate to the lung is 8.6 nL/s (= 0.0086 µL/s = 5.6 µl/10.8 min). For some experiments, a 2nd nebulization of 75 µL or 150 µL of

liquid was carried out keeping the animal ventilated while drying the ventilation tube between nebulizations. For these experiments a 1:16 polystyrene NPs and 1:5 iodine mixture in distilled water was used.

For nasal aspiration, a similar protocol was applied as reported by Gradl *et al.*[18]. Briefly, a mixture of polystyrene NPs (1:10 dilution) and gold NP (1:2 dilution) suspensions was loaded into a syringe pump mentioned above, permitting controlled liquid delivery outside the imaging hutch. Here 80 µL of the polystyrene-gold liquid mixture was spontaneously inhaled *via* the nose by the mouse. The PB-PCXI frame rate was maintained at 1.5 fps with the exposure time of 100 ms.

***In vivo* PB-PCXI**

All X-ray imaging experiments were carried out at an inverse Compton scattering source - the Munich Compact Light Source (MuCLS) located at the Technical University of Munich (TUM) in Garching, Germany. The source itself, was developed and installed by Lyncean Technologies Inc. (Fermont, USA)[54, 55], and the X-ray beamline infrastructure was designed and developed by TUM researchers. The source delivers a quasi-monochromatic and low divergence (4 mrad) X-ray beam. 25 keV X-rays with flux up to $2 \cdot 10^{10}$ ph/s were used. The principle behind propagation-based phase-contrast imaging is to use free space propagation of a partial spatial coherent beam (typically around 1 m) after penetrating a sample to introduce additional contrast. As the x-ray wavefield propagates from the sample to the detector the sample-associated phase modulations of the X-ray wavefront are converted into intensity modulations, which can be directly measured by a high-resolution X-ray detector. Here the propagation distance (sample-to-detector distance) was chosen to 1 m. There images were recorded by an Andor Zyla 5.5 sCMOS camera (2560 × 2160 pixels), combined with a 20 µm thick Gadox scintillator (Gd2O2S:Tb)

(CRYTUR, spol. s r.o., Czech Republic) deposited on a 2:1 fiber optic taper, resulting in 13 µm detector pixel-size. The source-to-sample distance was 4 m, leading to a geometric magnification of M = 1.25, an effective pixel size of 10.4 µm and a beam diameter of about 16 mm. As the X-ray beam has a fixed horizontal orientation, mice need to be positioned in a head-high position. Therefore, mice were placed in a specially designed mouse holder on a x-y-z rotation stage to facilitate positioning in the X-ray beam [31].

The pseudo-colored images in Figure 3-4 are a composition of the raw PB-PCXI images (gray scale) overlaid with the colored difference image[24], from which a pre-delivery image was subtracted to highlight the location of the contrast fluid similar to the analysis performed in Donnelley *et al.*[25]. Images were aligned before color coding via a cross-correlation based image registration.

***Ex vivo* lung tomography**

After intratracheal instillation or aerosolized delivery of one of the liquid NP susspensions described above, mice were sacrificed immediately by exsanguination while anaesthetized, the lung was transcardially perfused for blood removal and subsequently excised and either dried and inflated or optically cleared for subsequent *ex vivo* imaging (for a summary see Figure 1). Some of the excised lungs were mildly dried and inflated at a constant air pressure of 20-23 cm water in a microwave oven with the lowest power (10%). The lung tomography was performed on the excised, dried and inflated lung prior to fluorescence-based microscopy. 2049 projections over 360 degrees were captured and reconstructed with a standard flip-reconstruction analysis. The 3d data was rendered using AVIZO or Bitplane Imaris (http://www.bitplane.com/imaris/imaris).

Ex vivo tissue fluorescence imaging

Followed by CT scan of dried lungs, the *ex vivo* whole lung fluorescence imaging (WLFI) was performed using an IVIS (*in vivo* imaging system, Lumina II, Caliper/Perkin Elmer, USA) equipped with excitation/emission (ex/em) filters (ex/em = 640 nm/Cy5.5) suitable for the fluorescent NPs (SkyBlue). Subsequently, the dried lungs were embedded in polyurethane foam (PU foam Pattex Ultraweiss, Pattex, Germany) and sliced progressively perpendicular to the lung axis at an interval of 1 mm. After each slicing step, white light and fluorescence images of the block face and the 1 mm slice (Figure 3d) were recorded with the IVIS using ex/em = 640 nm/Cy5.5 filter. Similar IVIS imaging settings were used for all the lungs (exposure time = 2 s, binning = 1, field of view = 5, and f-stop = 1, this can be increased if saturated images occurred). Each 1 mm slice was imaged from both sides (top view and bottom view).

NP dosimetry for the iodine-NP treated (instilled and inhaled) lungs

The autofluorescence in each NP-treated lung was subtracted to yield absolute fluorescence intensity induced by SkyBlue NPs. 3 non-treated lungs were set as the background fluorescence and 4 typically fast-instilled lungs (50 µL 1:10 diluted or 100 µL 1:20 diluted SkyBlue NPs) were used to establish the intensity-dose standard curve for NP dosimetry (Figure S5). Note that for four regular instilled lungs the SkyBlue liquid was directly injected into the mouse lung via the trachea [27, 56], which is different from the protocol used for the slow-instilled lungs (*e.g.* 24 s for 100 µL liquid delivery). The fluorophore dose in a whole lung should be principally proportional to the sum of absolute fluorescence intensities from all 1 mm slices. After yielding the desired fluorescence intensity-dose conversion curve, quantitative measurement of the deposited dose in those lungs could be achieved. The left/right/whole lung deposition analysis

was carried out in the *ex vivo* WLFI data. The background intensity was subtracted to yield the absolute fluorescence intensity of SkyBlue for each part and the fluorophore intensity can be compared.

***Ex vivo* tissue-clearing LSFM**

Other non-dried lung samples were optically cleared with a modified version of the 3DISCO protocol[57] as described in our recent study[27]. Briefly, lung samples were dehydrated overnight in 10 ml of 50% v/v tetrahydrofuran/H_2O (THF, Sigma 186562- 1L), 50% THF/H_2O 1 h, 70% THF/H_2O 4 h, 80% THF/H_2O 4 h, 100% THF 1 h, 100% THF overnight, and 100%THF 1 h with slightly shaking. Samples were gently dried and then incubated in dichloromethane (DCM, Sigma 270997-1 L) around 30 min until they sank to the bottom. Finally, samples were incubated without shaking in dibenzyl ether (DBE, Sigma 108014-1KG) for at least 2 h until imaging and then stored in DBE at room temperature.

Lung samples were scanned with a light sheet fluorescence microscope (LSFM, Ultramicroscope II, LaVision Biotec) equipped with a sCMOS camera (Andor Neo) and a 2× objective lens (Olympus MVPLAPO 2×/0.5 NA) equipped with an Olympus MVX-10 zoom body, which provided zoom-out and –in ranging from 0.63x up to 6.3x. For the whole lung imaging, light sheet scans were generated with 0.63× zoom magnification with individual ex/em bandpass filters for melamine NPs (ex/em=640(30) nm / 690(50) nm)and QDs (ex/em=640(30) nm / 795(50) nm) with a step size of 10 μm. Tissue autofluorescence was imaged under the ex/em=545(30) nm / 605(70) nm filters. Samples were typically imaged with an exposure time of 150 ms, at a full laser power with the light sheet by adjusting xy width and numerical aperture

(NA) to the sample size. High magnification scans (*e.g.* 8× in figure 6e and f) were usually performed with a step size of 4 μm. The imaging chamber was filled with DBE.

Image processing and analysis

All (X-ray and CT) images were flat field and dark current corrected. X-ray images were analyzed and the dynamic NP delivery videos were generated using ImageJ (https://imagej.nih.gov/ij/). Fluorescence images scanned by IVIS consisting of whole lung images and dried lung slices and their corresponding NP dosimetry analysis were performed with the Living Imaging 4.0 Software (Caliper). The 3D images with maximum intensity projection and videos with 3D manipulation scanned by LSFM were processed using Bitplane Imaris. All data were presented as mean ± STD and *, **, and *** refer to statistically significant differences $P < 0.05$, $P < 0.01$, and $P < 0.001$, respectively and plotted using SigmaPlot version 12.0 (Systat Software GmbH, Germany). $N \geq 3$.

Supporting information

Supporting Information is available from the Wiley Online Library or from the author.

Supporting videos

Video S1 and S2: Dynamic process of delivery of iodine-NP suspension (100 µL) to the *left* and *whole* lung of mice via intratracheal slow-instillation obtained by *in vivo* PB-PCXI, respectively.

Video S3: Targeted delivery of iodine-NP suspension (100 µL) to the *right* half of a mouse lung with an overlaid pseudo-color dose image highlighting the dynamics of the delivery process imaged by *in vivo* PB-PCXI.

Video S4: 3D whole lung reconstruction reveals the predominately right lung distribution pattern of iodine-NP liquid generated from *ex vivo* CT (same lung as Video S3).

Video S5 and S6: *In vivo* PB-PCXI shows time-resolved visualization of small-volume (4 µL) intratracheal slow-instillation of iodine-NP suspension in the absence and presence of alveolar surfactant, respectively.

Video S7: Nasal aspiration delivery of gold NPs (40 µL) into a mouse respiratory tract observed by *in vivo* PB-PCXI.

Video S8 and S9: *In vivo* PB-PCXI shows the temporal profile of iron oxide particles (mixed with melamine NP) and QDs applied intratracheal slow-instillation (100 µL) to the mouse lungs.

Video S10: 3D whole-lung distribution profiles of QDs after intratracheal slow-instillation (100 µL) obtained by *ex vivo* LSFM (lung tissue in green and QDs in red).

Video S11: Time-resolved visualization of 150 µL iodine-NP aerosol delivery to the mouse lung during ventilator-assisted aerosol inhalation imaged by *in vivo* PB-PCXI.

Video S12: Tracking NP deposition (green) in the bronchial tree of a mouse lung (red) after ventilator-assisted aerosol inhalation scanned by *ex vivo* LSFM.

Notes

The authors declare no competing financial interest.

ACKNOWLEDGMENTS

The authors thank Lyncean Technologies Inc. for the technical support of the compact synchrotron light source. We acknowledge financial support through the Centre for Advanced Laser Applications (CALA), and the DFG Gottfried Wilhelm Leibniz program. This research was (partially) supported through the EU Horizon 2020 project SmartNanoTox, grant agreement no. 686098. We thank the China Scholarship Council (CSC) for providing the fellowship for L.Y. (201506820008). KM was supported by a Veski VPRF, ARC FT180100374 and NHRMC GNT1140617, and KM, RG and FP completed this work with the support of the TUM Institute for Advanced Study, funded by the German Excellence Initiative and the European Union Seventh Framework Program under grant agreement no 291763 and co-funded by the European Union. MDo supported by NHMRC project GNT1160011, and by a Robinson Research Institute Career Development Fellowship. We thank Juliana Martins de Silva for the production of the gold NPs.

References

1. WHO. (2018). The Top 10 Causes of Death. Accessed: May. 24, **2018**. [Online]. Available: https://www.who.int/news-room/fact-sheets/detail/the-top-10-causes-of-death
2. W. H. Lee,C. Y. Loo,D. Traini,P. M. Young, *Asian J Pharm Sci* **2015,** *10*, 481-489.
3. M. B. Dolovich,R. Dhand, *Lancet* **2011,** *377*, 1032-45.
4. S. Azarmi,W. H. Roa,R. Lobenberg, *Adv Drug Deliv Rev* **2008,** *60*, 863-75.
5. C. Loira-Pastoriza,J. Todoroff,R. Vanbever, *Adv Drug Deliv Rev* **2014,** *75*, 81-91.
6. J. Liu,R. Zhang,Z. P. Xu, *Small* **2019**, e1900262.
7. J. Shi,P. W. Kantoff,R. Wooster,O. C. Farokhzad, *Nat Rev Cancer* **2017,** *17*, 20-37.
8. M. Doroudian,R. MacLoughlin,F. Poynton,A. Prina-Mello,S. C. Donnelly, *Thorax* **2019**.
9. S. Wilhelm,A. J. Tavares,Q. Dai,S. Ohta,J. Audet,H. F. Dvorak,W. C. W. Chan, *Nat Rev Mater* **2016,** *1*.
10. S. Kunjachan,J. Ehling,G. Storm,F. Kiessling,T. Lammers, *Chem Rev* **2015,** *115*, 10907-37.
11. B. Pelaz,C. H. Alexiou,R. A. Alvarez -Puebla,F. Alves,A. M. Andrews,S. Ashraf,L. P. Balogh,L. Ballerini,A. Bestetti,C. Brendel,S. Bosi,M. Carril,W. C. W. Chan,C. Y. Chen,X. D. Chen,X. Y. Chen,Z. Cheng,D. X. Cui,J. Z. Du,C. Dullin,A. Escudero,N. Feliu,M. Y. Gao,M. George,Y. Gogotsi,A. Grunweller,Z. W. Gu,N. J. Halas,N. Hampp,R. K. Hartmann,M. C. Hersam,P. Hunziker,J. Jian,X. Y. Jiang,P. Jungebluth,P. Kadhiresan,K. Kataoka,A. Khademhosseini,J. Kopecek,N. A. Kotov,H. F. Krug,D. S. Lee,C. M. Lehr,K. W. Leong,X. J. Liang,M. L. Lim,L. M. Liz-Marzan,X. M. Ma,P. Macchiarini,H. Meng,H. Mohwald,P. Mulvaney,A. E. Nel,S. M. Nie,P. Nordlander,T. Okano,J. Oliveira,T. H. Park,R. M. Penner,M. Prato,V. Puntes,V. M. Rotello,A. Samarakoon,R. E. Schaak,Y. Q. Shen,S. Sjoqvist,A. G. Skirtach,M. G. Soliman,M. M. Stevens,H. W. Sung,B. Z. Tang,R. Tietze,B. N. Udugama,J. S. VanEpps,T. Weil,P. S. Weiss,I. Willner,Y. Z. Wu,L. L. Yang,Z. Yue,Q. Zhang,Q. Zhang,X. E. Zhang,Y. L. Zhao,X. Zhou,W. J. Parak, *ACS Nano* **2017,** *11*, 2313-2381.
12. J. Biederer,S. Mirsadraee,M. Beer,F. Molinari,C. Hintze,G. Bauman,M. Both,E. J. Van Beek,J. Wild,M. Puderbach, *Insights Imaging* **2012,** *3*, 373-86.
13. C. Hoyer,N. Gass,W. Weber-Fahr,A. Sartorius, *Neuropsychobiology* **2014,** *69*, 187-201.
14. M. Eghtedari,A. Oraevsky,J. A. Copland,N. A. Kotov,A. Conjusteau,M. Motamedi, *Nano Lett* **2007,** *7*, 1914-8.
15. A. Taruttis,V. Ntziachristos, *Nat Photonics* **2015,** *9*, 219-227.
16. M. Donnelley,K. S. Morgan,K. K. Siu,D. W. Parsons, *J Aerosol Med Pulm Drug Deliv* **2013,** *26*, 307-16.
17. L. Porra,L. Degrugilliers,L. Broche,G. Albu,S. Strengell,H. Suhonen,G. H. Fodor,F. Petak,P. Suortti,W. Habre,A. R. A. Sovijarvi,S. Bayat, *Sci Rep* **2018,** *8*, 3519.
18. R. Gradl,M. Dierolf,B. Gunther,L. Hehn,W. Moller,D. Kutschke,L. Yang,M. Donnelley,R. Murrie,A. Erl,T. Stoeger,B. Gleich,K. Achterhold,O. Schmid,F. Pfeiffer,K. S. Morgan, *Sci Rep* **2018,** *8*, 6788.
19. F. G. Meinel,F. Schwab,S. Schleede,M. Bech,J. Herzen,K. Achterhold,S. Auweter,F. Bamberg,A. O. Yildirim,A. Bohla,O. Eickelberg,R. Loewen,M. Gifford,R. Ruth,M. F. Reiser,F. Pfeiffer,K. Nikolaou, *PLoS One* **2013,** *8*, e59526.
20. S. Aryal,J. Key,C. Stigliano,M. D. Landis,D. Y. Lee,P. Decuzzi, *Small* **2014,** *10*, 2688-96.
21. N. Karra,T. Nassar,A. N. Ripin,O. Schwob,J. Borlak,S. Benita, *Small* **2013,** *9*, 4221-36.
22. C. Xu,P. Wang,J. Zhang,H. Tian,K. Park,X. Chen, *Small* **2015,** *11*, 4321-33.
23. C. S. Schneider,Q. G. Xu,N. J. Boylan,J. Chisholm,B. C. Tang,B. S. Schuster,A. Henning,L. M. Ensign,E. Lee,P. Adstamongkonkul,B. W. Simons,S. Y. S. Wang,X. Q. Gong,T. Yu,M. P. Boyle,J. S. Suk,J. Hanes, *Sci Adv* **2017,** *3*.
24. R. Gradl,M. Dierolf,L. Yang,L. Hehn,B. Gunther,W. Moller,D. Kutschke,T. Stoeger,B. Gleich,K. Achterhold,M. Donnelley,F. Pfeiffer,O. Schmid,K. S. Morgan, *J Control Release* **2019**.

25. M. Donnelley,K. K. Siu,R. A. Jamison,D. W. Parsons, *Gene Ther* **2012,** *19*, 8-14.
26. M. Donnelley,K. S. Morgan,K. K. W. Siu,D. W. Parsons, *J Synchrotron Radiat* **2012,** *19*, 551-558.
27. L. Yang,A. Feuchtinger,W. Moller,Y. Ding,D. Kutschke,G. Moller,J. C. Schittny,G. Burgstaller,W. Hofmann,T. Stoeger,R. Daniel,A. Walch,O. Schmid, *ACS Nano* **2019,** *13*, 1029-1041.
28. D. Yi,A. Price,A. Panoskaltsis-Mortari,A. Naqwi,T. S. Wiedmann, *Anal. Biochem.* **2010,** *403*, 88-93.
29. N. Barapatre,P. Symvoulidis,W. Moller,F. Prade,N. C. Deliolanis,S. Hertel,G. Winter,A. O. Yildirim,T. Stoeger,O. Eickelberg,V. Ntziachristos,O. Schmid, *J. Pharm. Biomed. Anal.* **2015,** *102*, 129-36.
30. E. J. Veldhuizen,H. P. Haagsman, *Biochim Biophys Acta* **2000,** *1467*, 255-70.
31. K. S. Morgan, D. Parsons, P. Cmielewski, A. McCarron, R. Gradl, N. Farrow, K. Siu, A. Takeuchi, Y. Sukuzi, K. Uesugi, M. Uesugi, N. Yagi, C. Hall, M. Klein, A. Maksimenko, A. Stevenson, D. Hausermann, M. Dierolf, F.Pfeiffer, M. Donnelley, unpublished.
32. H. Lusic,M. W. Grinstaff, *Chem Rev* **2013,** *113*, 1641-66.
33. J. C. De La Vega,U. O. Hafeli, *Contrast Media Mol I* **2015,** *10*, 81-95.
34. S. H. van Rijt,D. A. Bolukbas,C. Argyo,K. Wipplinger,M. Naureen,S. Datz,O. Eickelberg,S. Meiners,T. Bein,O. Schmid,T. Stoeger, *Nanoscale* **2016,** *8*, 8058-8069.
35. S. Hussain,J. Joo,J. Kang,B. Kim,G. B. Braun,Z. G. She,D. Kim,A. P. Mann,T. Molder,T. Teesalu,S. Carnazza,S. Guglielmino,M. J. Sailor,E. Ruoslahti, *Nat Biomed Eng* **2018,** *2*, 95-103.
36. P. Muralidharan,M. Malapit,E. Mallory,D. Hayes, Jr.,H. M. Mansour, *Nanomedicine* **2015,** *11*, 1189-99.
37. F. S. Collins,H. Varmus, *N Engl J Med* **2015,** *372*, 793-5.
38. O. Schmid,T. Stoeger, *J. Aerosol Sci.* **2016,** *99*, 133-143.
39. K. Ganguly,D. Ettehadieh,S. Upadhyay,S. Takenaka,T. Adler,E. Karg,F. Krombach,W. G. Kreyling,H. Schulz,O. Schmid,T. Stoeger, *Part. Fibre Toxicol.* **2017,** *14*.
40. X. Duan,Y. Li, *Small* **2013,** *9*, 1521-32.
41. L. Yang,H. Kuang,W. Zhang,Z. P. Aguilar,H. Wei,H. Xu, *Sci. Rep.* **2017,** *7*, 3303.
42. O. Schmid,F. R. Cassee, *Part. Fibre Toxicol.* **2017,** *14*.
43. B. Drasler,D. Vanhecke,L. Rodriguez-Lorenzo,A. Petri-Fink,B. Rothen-Rutishauser, *Nanomedicine* **2017,** *12*, 1095-1099.
44. D. Vanhecke,L. Rodriguez-Lorenzo,M. J. D. Clift,F. Blank,A. Petri-Fink,B. Rothen-Rutishauser, *Nanomedicine* **2014,** *9*, 1885-1900.
45. R. Sekine,K. L. Moore,M. Matzke,P. Vallotton,H. Jiang,G. M. Hughes,J. K. Kirby,E. Donner,C. R. M. Grovenor,C. Svendsen,E. Lombi, *ACS Nano* **2017,** *11*, 10894-10902.
46. H. Y. Kim,R. Li,T. S. C. Ng,G. Courties,C. B. Rodell,M. Prytyskach,R. H. Kohler,M. J. Pittet,M. Nahrendorf,R. Weissleder,M. A. Miller, *Acs Nano* **2018,** *12*, 12015-12029.
47. M. Donnelley,K. K. W. Siu,K. S. Morgan,W. Skinner,Y. Suzuki,A. Takeuchi,K. Uesugi,N. Yagi,D. W. Parsons, *J Synchrotron Radiat* **2010,** *17*, 719-729.
48. M. Donnelley,K. S. Morgan,K. K. Siu,N. R. Farrow,C. S. Stahr,R. C. Boucher,A. Fouras,D. W. Parsons, *Sci Rep* **2014,** *4*, 3689.
49. M. Donnelley,K. S. Morgan,M. Awadalla,N. R. Farrow,C. Hall,D. W. Parsons, *Respir Res* **2017,** *18*, 95.
50. M. Donnelley,K. S. Morgan,A. Fouras,W. Skinner,K. Uesugi,N. Yagi,K. K. Siu,D. W. Parsons, *J Synchrotron Radiat* **2009,** *16*, 553-61.
51 W. G. Kreyling,S. Hirn,W. Moller,C. Schleh,A. Wenk,G. Celik,J. Lipka,M. Schaffler,N. Haberl,B. D. Johnston,R. Sperling,G. Schmid,U. Simon,W. J. Parak,M. Semmler-Behnke, *Acs Nano* **2014**, *8*, 222-233.
52. H. S. Choi,Y. Ashitate,J. H. Lee,S. H. Kim,A. Matsui,N. Insin,M. G. Bawendi,M. Semmler-Behnke,J. V. Frangioni,A. Tsuda, *Nat. Biotechnol* **2010**, *28*, 1300

53. J. Harrison,C. A. Bartlett,G. Cowin,P. K. Nicholls,C. W. Evans,T. D. Clemons,B. Zdyrko,I. A. Luzinov,A. R. Harvey,K. S. Iyer,S. A. Dunlop,M. Fitzgerald, *Small* **2012,** *8*, 1579-89.
54. E. Eggl,M. Dierolf,K. Achterhold,C. Jud,B. Gunther,E. Braig,B. Gleich,F. Pfeiffer, *J Synchrotron Radiat* **2016,** *23*, 1137-42.
55. K. Achterhold,M. Bech,S. Schleede,G. Potdevin,R. Ruth,R. Loewen,F. Pfeiffer, *Sci Rep* **2013,** *3*, 1313.
56. A. A. Gotz,J. Rozman,H. G. Rodel,H. Fuchs,V. Gailus-Durner,M. H. de Angelis,M. Klingenspor,T. Stoeger, *Part. Fibre Toxicol.* **2011,** *8*.
57. A. Erturk,K. Becker,N. Jahrling,C. P. Mauch,C. D. Hojer,J. G. Egen,F. Hellal,F. Bradke,M. Sheng,H. U. Dodt, *Nat. Protoc.* **2012,** *7*, 1983-95.

Figures

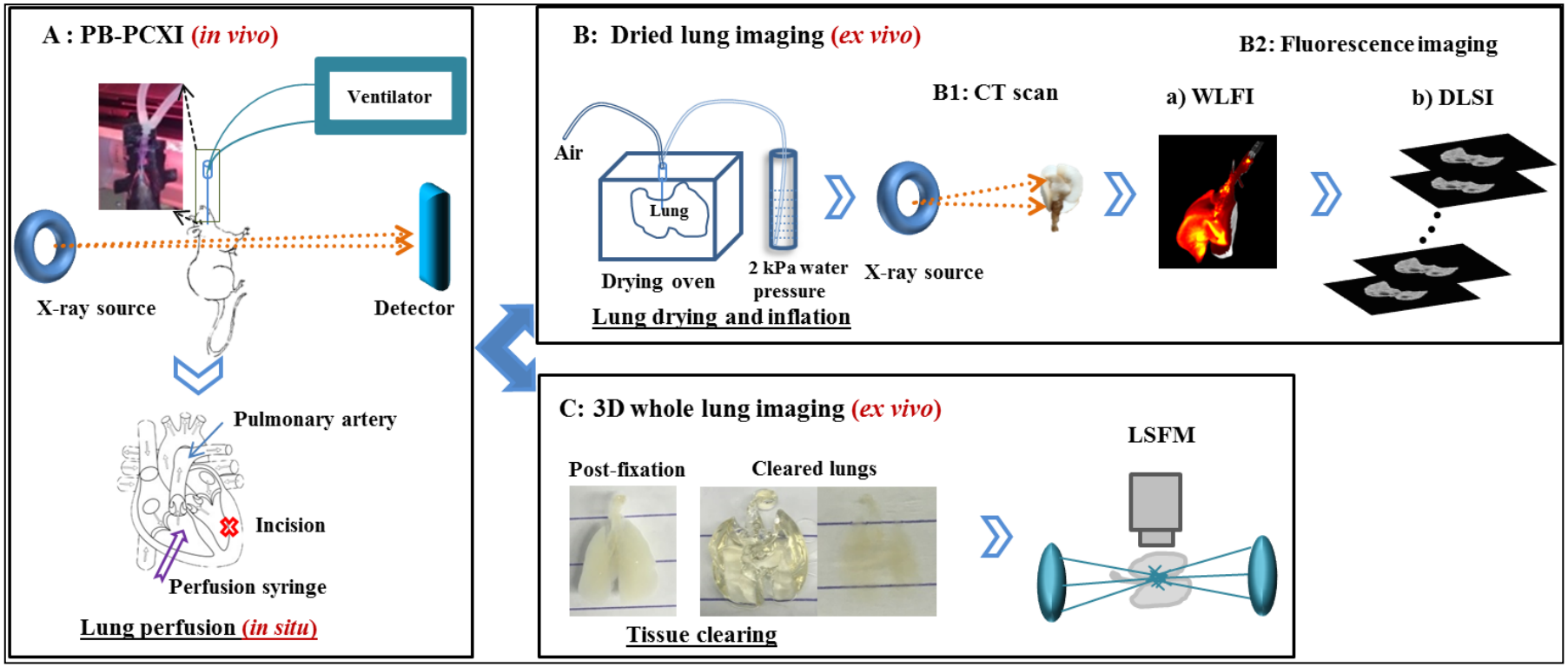

Figure 1: Schematic workflow of multimodal imaging platform from *in vivo* propagation-based phase contrast X-ray imaging (PB-PCXI) to either *ex vivo* light sheet fluorescence microscopy (LSFM) or *ex vivo* lung slice fluorescence imaging (LSFI). Those imaging processes involved in the data acquisition (*in vivo* PB-PCXI, *ex vivo* computed tomography (CT), *ex vivo* whole lung fluorescence imaging (WLFI) and LSFI, and *ex vivo* LSFM) and sample processing (*in situ* lung perfusion, *ex vivo* lung drying and inflation, and *ex vivo* lung tissue clearing) were applied in this study.

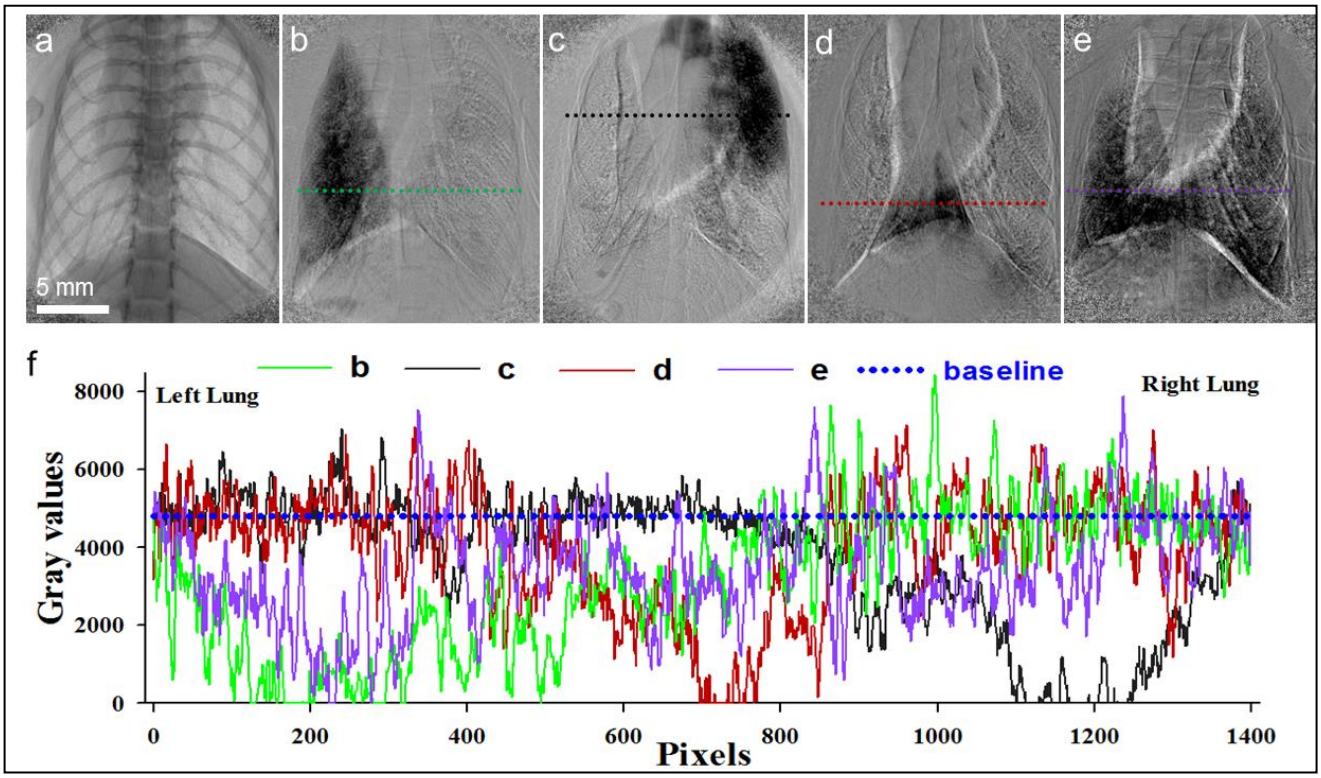

Figure 2: Controlled iodine-nanoparticle liquid delivery to left/right or whole lung via slow-instillation can be visualized *in vivo* using PB-PCXI. (a): A raw X-ray image directly captured during instillation of 100 µL iodine-polystyrene NP liquid to the mouse lung. (b): Same as panel a, but a pre-delivery image is subtracted, clearly enhancing the visibility of the iodine-polystyrene NP liquid in the left half of the lung. (c), (d), and (e) are difference images as well, but for different experiments delivering the iodine-polystyrene NP liquid to the upper right lung, lower right lung, and entire lung, respectively, by controlling the position/depth of intubation cannula. (f): Pixel-by-pixel intensity profiles along the linear trajectories across the 2D lung images (along the colored dashed lines figure 2b, c, d, and e) demonstrate that massive decreases in pixel intensity (compared to baseline in blue) result from the substantial deposition of iodine, while the fluctuations in the signal are due to *e.g.* imperfect subtraction of the pre-delivery image.

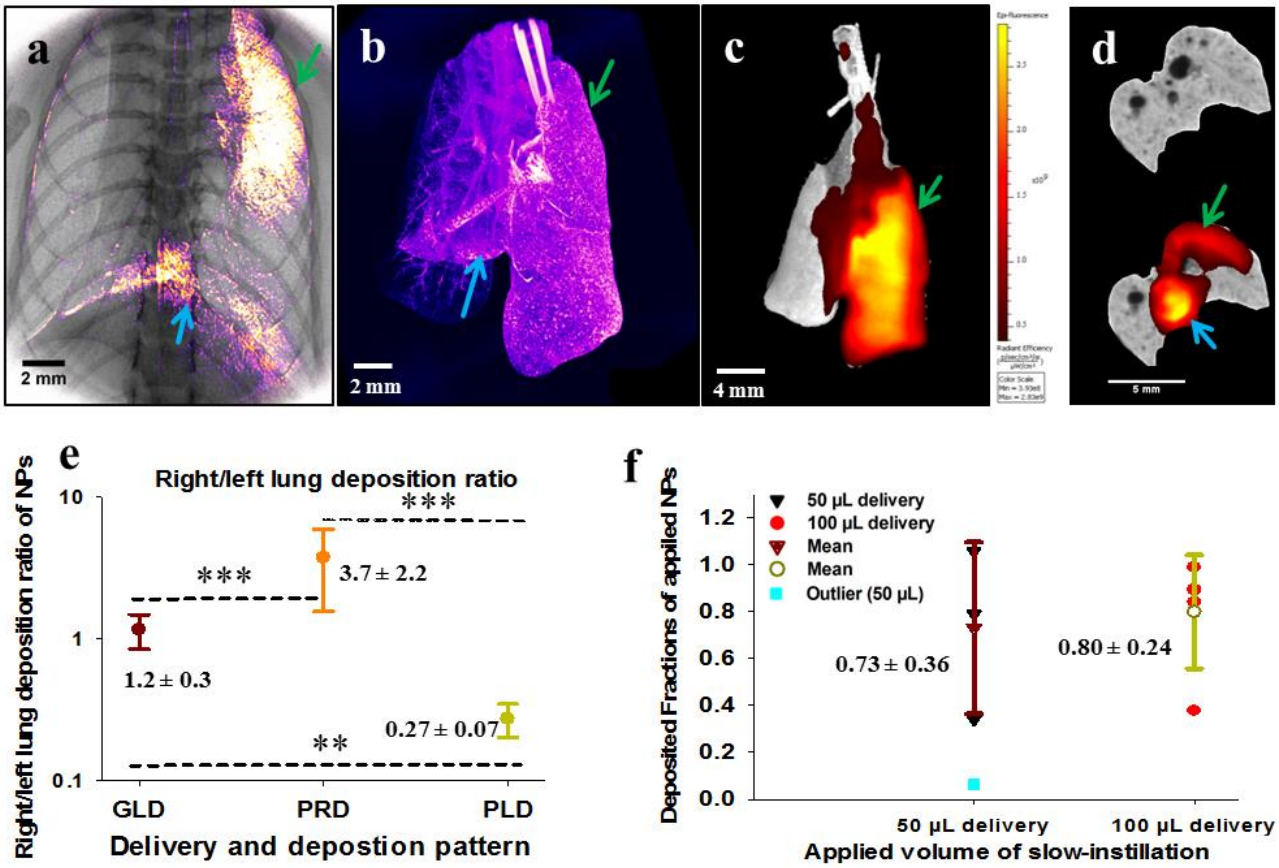

Figure 3: *In vivo* and *ex vivo* imaging modalities show consistent end-delivery distribution of an intratracheally slow-instilled iodine-nanoparticle suspension in the lungs (posterior view). (a): A pseudo-coloured difference image (analogous to Figure 2b) overlaid with a directly obtained X-ray image (analogous to Figure 2a) allows for co-mapping of lung morphology and iodine-polystyrene NP deposition, indicating preferential delivery to the superior and post-caval lobe of the right lung (green and blue arrow, respectively). (b): Matching bi-lobal delivery was also observed from an *ex vivo* CT scan. *Ex vivo* fluorescence images obtained from WLFI (c) and LSFI (d) further indicate the success of right lung delivery. Due to tissue-induced light attenuation, the fluorescence signal from the near diaphragm post-caval lobe is not visible in posterior view (c) but clearly evident in anterior view (Figure S2c). (e): Right/left deposition ratios of NPs normalized to the respective right/left lung volume ratio were measured quantitatively with WLFI, displaying the success of preferential right or left delivery (PRD or PLD) and global lung delivery (GLD). (f): Quantitative determination of the dose/volume of liquid delivered to the whole-lung using the LSFI data for 50 or 100 µL of applied liquid.

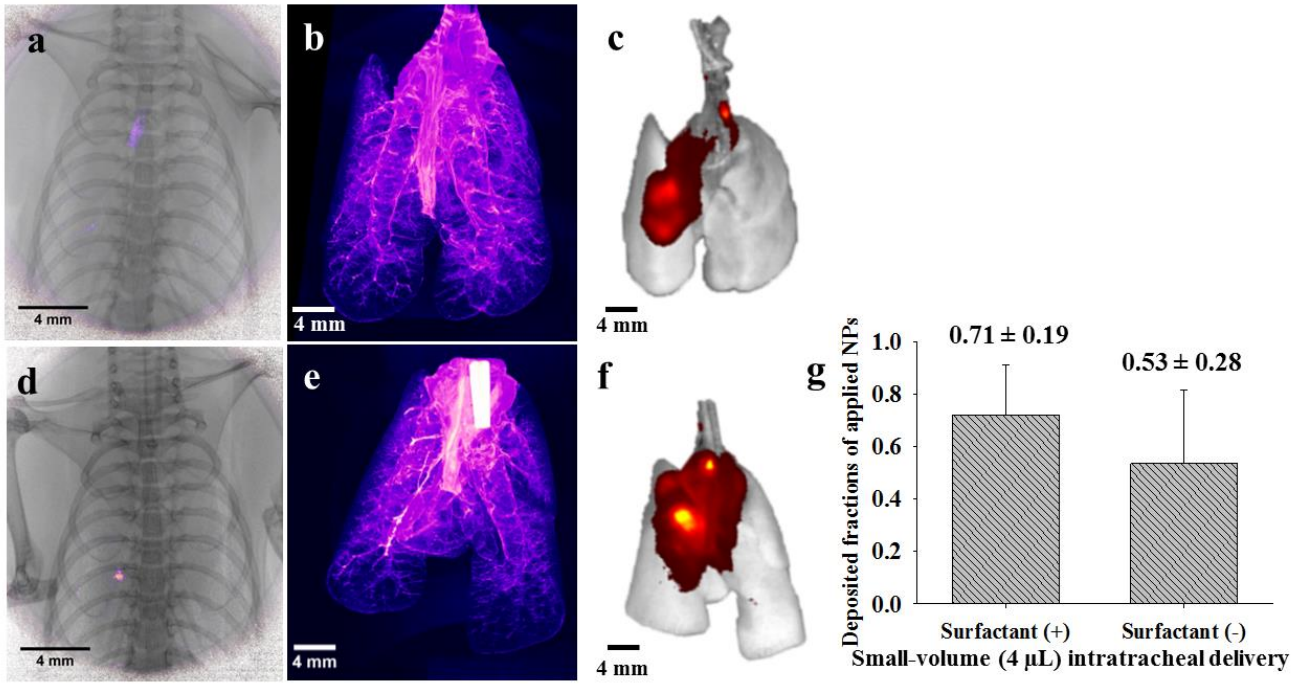

Figure 4: Determination of small-volume (4 µL) intratracheal slow-instillation of iodine-NP suspension in the absence (a, b, and c) and presence (d, e, and f) of alveolar surfactant by multimodal imaging. Representative 2D images with *in vivo* PB-PCXI show the highly localized delivery of 4µL iodine-polystyrene NP liquid without (a) or with (d) surfactant. The x-ray signal is below the detection limit of 3D reconstructed images from *ex vivo* CT (b and e), while 2D images obtained from *ex vivo* WLFI exhibit the proximal bronchial distribution of iodine-polystyrene NP liquid (c and f), albeit more diffuse then in a) and d) due to tissue-induced light scattering. The presence of surfactant had no effect on the speed of liquid dispersion and uniformity of distribution. (g): The deposited fractions of 4 µL slow-instillation without or with surfactant based on LSFI data.

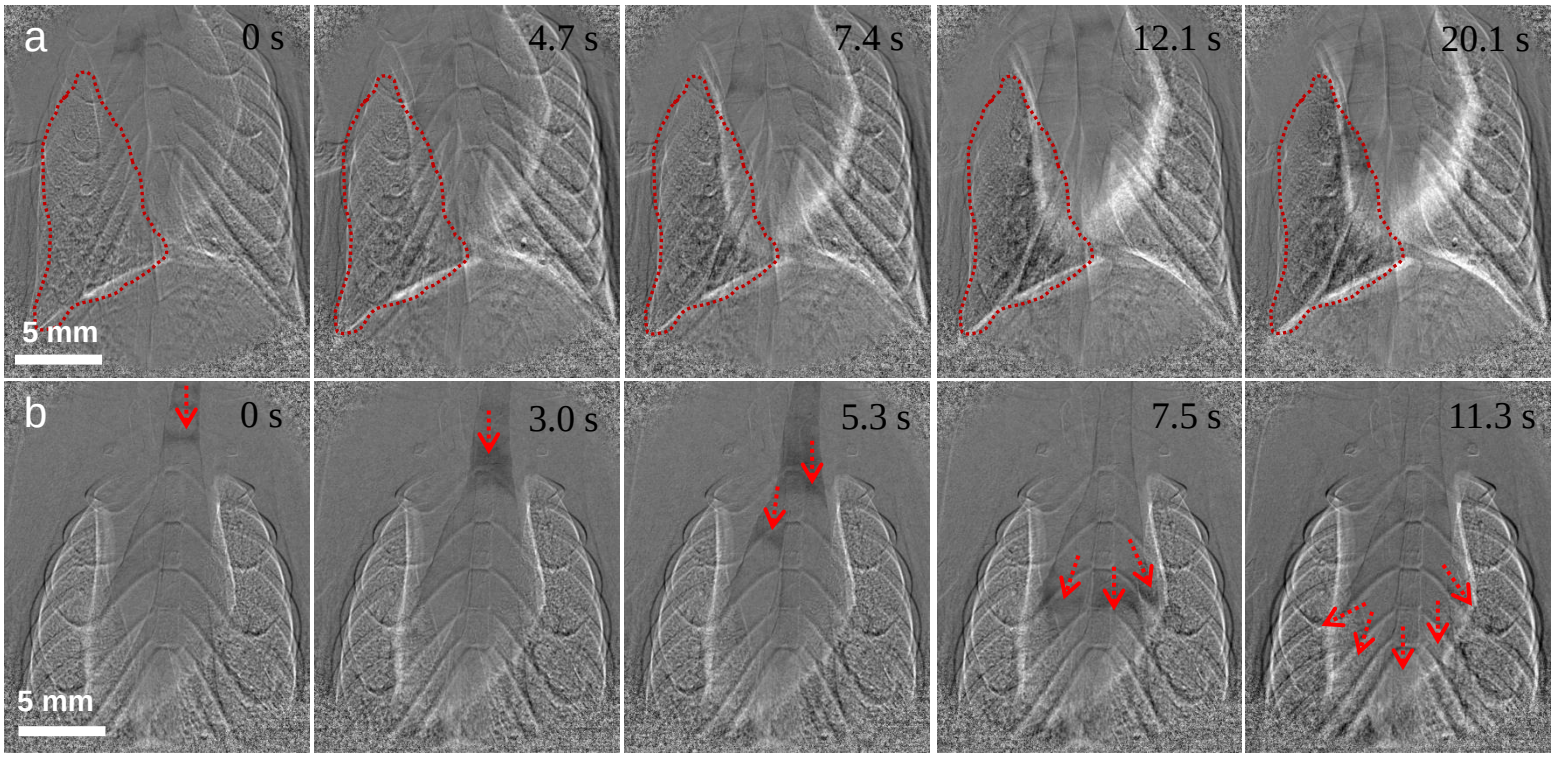

Figure 5: Real-time monitoring of pulmonary delivery of pure particles by *in vivo* PB-PCXI. (a) and (b) show difference image sequences of the intratracheal slow-instillation of 100 µL iron oxide (mixed with fluorescent melamine NPs) and pure QDs at 24 s (4.2 µL/s) to the mouse lung, respectively. The iron oxide particles were delivered quite uniformly throughout the left lung (results from placing the intubation cannula beyond the first bifurcation) (a) and QDs were distributed to the whole lung (b). Compared to iodine the reduced image contrast is in part due to the lower delivered particle dose. Arrows indicate the formation of liquid accumulations which do not completely block the airways (no secondary aerosol formation) but gradually slide down the airway tree. The increased background noise (*e.g.* rib cage morphology) is due to unavoidable mouse movements and the lower contrast of pure NPs as compared to iodine. The time axis indicates real time in seconds after the first image in which time was set to 0 s.

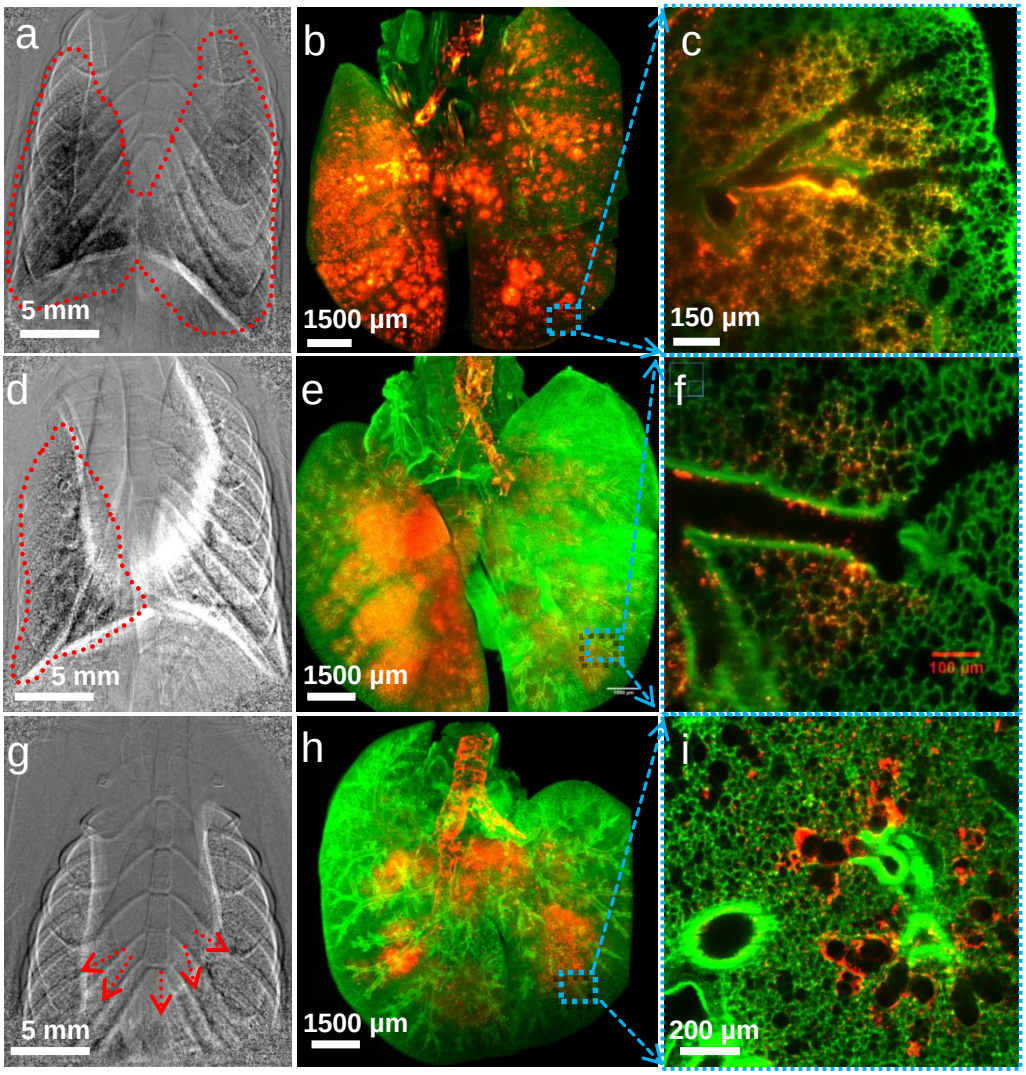

Figure 6: *In vivo* PB-PCXI and *ex vivo* tissue-cleared LSFM for cellular-resolution visualization of NP-liquid localization in non-dissected whole murine lungs after slow-instillation (100 µL of liquid). The PB-PCXI difference image (a) shows the pulmonary distribution of an iodine-melamine NP suspension after instillation, which is consistent with the result obtained from 3D reconstructed LSFM image (b). A 2D image with cellular resolution (c) further reveals the specific NP localization. Images obtained from *in vivo* PB-PCXI (d) and *ex vivo* LSFM (e) distinctly show preferential left lung distribution of a mixture of iron oxide particles with melamine resin NPs. (f): NP deposition in distal small airways (bronchioles) and proximal alveolar regions was revealed by 2D images in single cell resolution. For QD application a similar set of images (g, h and i) shows that QDs were delivered to all 5 lobes with highest deposition in the distal part of the terminal bronchioles and the entrance of the alveolar duct. Green: tissue autofluorescence; Red: melamine NPs (b, c, e, and f) or QDs (h and i).

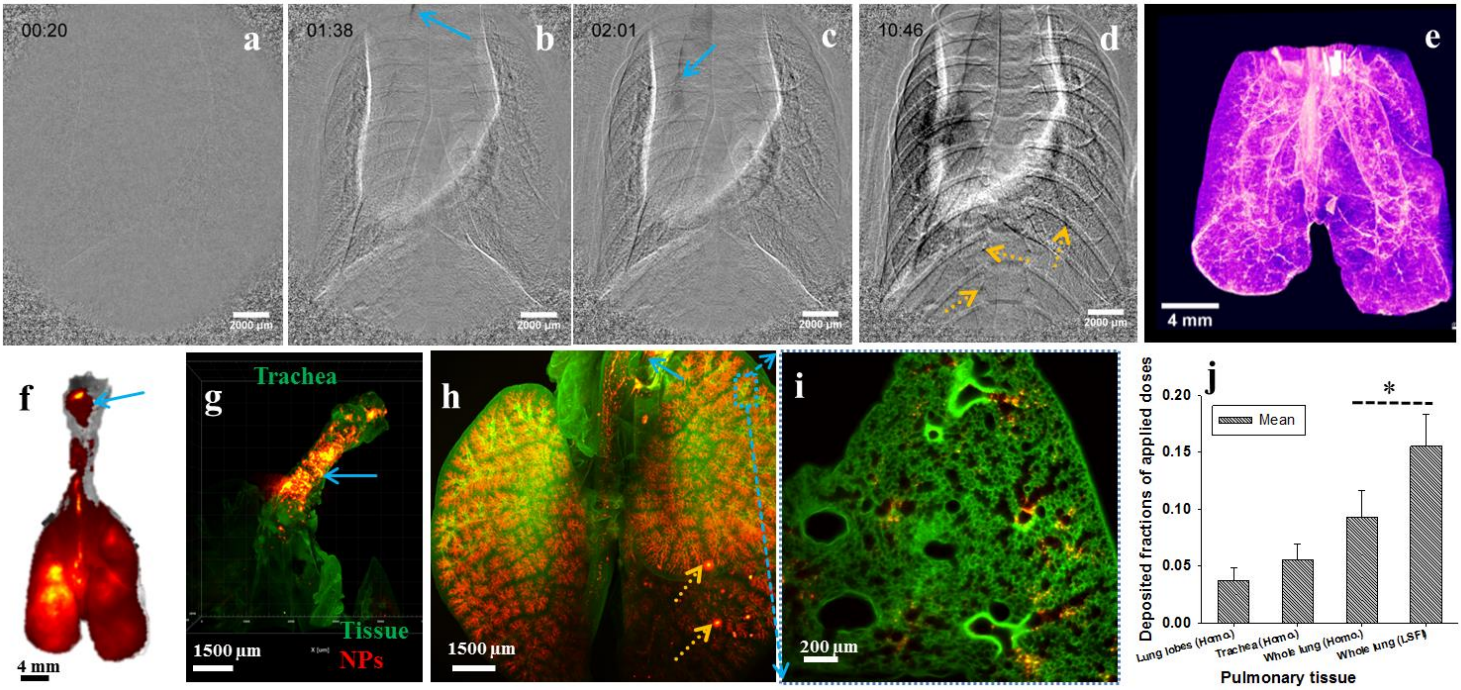

Figure 7: Leveraging multi-modal imaging for a comprehensive understanding of the characteristics and delivery mechanism of ventilator-assisted aerosol inhalation. Time-resolved visualization of 150 µL aerosol inhalation (takes 10 min 48 s) with *in vivo* PB-PCXI shows no obvious X-ray signals during the entire period of aerosol delivery (iodine-polystyrene NP suspension) (a). However, occasional appearance of localized accumulations of liquid could be observed in the upper airways (b, light blue arrow), which were then gradually transported to the lower airways (c, light blue arrow) and finally dispersed in the bronchiolar region (d, yellow arrows). a-d: The time (mm:ss) noted in the left upper corner of the images indicate the time after start of aerosol inhalation. The 3D and 2D images from *ex vivo* CT (e) and WLFI (f), respectively, exhibit the whole lung liquid distribution, but only WLFI provides a differentiated deposition profile matching, end-inhalation PB-PCXI. The LSFM images (g-i), which were obtained for a different lung after aerosol inhalation of 40 µL melamine NP suspension, show high deposition at the end of the intubation cannula in the trachea (g) and very uniform deposition throughout all lung lobes (h) especially in the proximal acinar region (bronchioles and proximal part of alveolar duct) with the exception of a few "hot spots" in the bronchioles (h, yellow arrow), which can be rationalized by the features (blue arrows) observed by PB-PCXI (d). (i): 2D cellular visualization of NP deposition in lung tissue. (j): Determination of the deposited fraction of the applied aerosol dose in all lung lobes, trachea and whole lung (lung lobes + trachea) using quantitative spectrofluorometry in lung homogenates (homo) or on lung slices (LSFI).

Table 1: Main characteristics and hence complementarity of the propagation-based phase contrast X-ray imaging (PB-PCXI), computed tomography (CT), whole lung fluorescence imaging (WLFI), lung slice fluorescence imaging (LSFI), and light sheet fluorescence microscopy (LSFM) at a glance. Strengths are graded low (+) to high (+++).

Imaging method	*In Vivo*/ *Ex Vivo*	Dimension	Resolution	Fidelity	Anatomical information	Dosimetry	Technical complexity	Contrast agents
PB-PCXI	*In vivo*	2D + time	+	+++	+	++	+++	Iodine[M1], Iron oxide particles[M2], Gold NPs, Quantum dots (QD)
CT	*Ex vivo*	3D	++	+++	++	+	++	
WLFI	*Ex vivo*	<2D[§]	+	++	+	++	+	Sky Blue NPs[M1], Melamine NPs[M1,2], Quantum dots
LSFI	*Ex vivo*	2D/3D	+	++	++	+++	++	
LSFM	*Ex vivo*	2D/3D	+++	++	+++	+++	++	

M1: mixture 1(iodine + Sky Blue NPs/melamine NPs); M2: mixture 2 (iron oxide+melamine NPs).
§ Penetration depth is ca. 1 mm (depending on wavelength) – only fraction of murine lung is imaged

Table of Content

The multimodal *in vivo*/*ex vivo* imaging platform established here provides comprehensive insights into the dynamic process of pulmonary nanoparticle delivery with high temporal and quantitative three-dimensional spatial resolution in the entire mouse lungs.

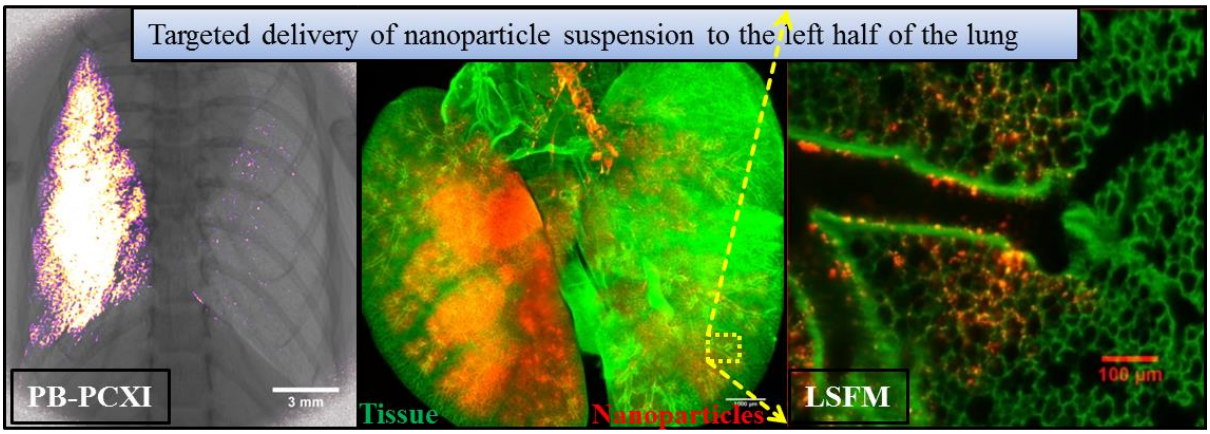

Keyword: Dynamic lung imaging of nanoparticle delivery